Ocean Engineering 313 (2024) 119548

Contents lists available at ScienceDirect

Ocean Engineering

journal homepage: www.elsevier.com/locate/oceaneng

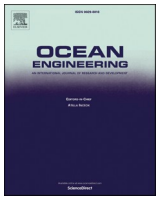

Research paper

Numerical investigation of the effects of short-crested irregular waves on the performance of a floating power capture platform

Haitao Wu, Zhiming Yuan *

Department of Naval Architecture, Ocean and Marine Engineering, University of Strathclyde, Glasgow, G4 0LZ, United Kingdom

ARTICLE INFO

Keywords:
Floating power capture platform
Semi-submersible platform
Wave energy converter
Short-crested irregular waves
Dynamic behavior

ABSTRACT

This paper presents a novel power capture platform concept consisting of a semi-submersible platform and multiple point-absorber wave energy converters (WECs). The primary objective of the current study is to investigate the dynamic behavior of the power capture platform under short-crested irregular wave conditions. A spreading function is used to modify the JONSWAP spectrum into a wave spectrum that accounts for both frequency and direction. To ensure the reliability of the numerical analysis, three-dimensional potential flow theory and boundary element method (BEM) are utilized to perform mesh convergence analysis and hydrodynamic validation of the platform and WEC models. Time-domain simulations are conducted to evaluate the effects of wave directionality on the platform motion, mooring line tension, and power absorption of the WEC array. In addition, three models, "single WEC", "WEC array" and "fixed power capture platform" are defined. The influence of hydrodynamic interactions and platform motion are predicted by comparing the power absorption of individual WEC, WEC row, and WEC array among these models. The results show that the effects of wave directionality on the performance of the floating power capture platform cannot be ignored. The findings of this study may provide some insights into the design of power capture platforms. Meanwhile, it is recommended to determine the wave characteristics of the target operational area in advance, in order to find out the optimal design for system stability and power absorption.

1. Introduction

Compared to wind, tidal and solar energy, wave energy is considered to be more promising because of its higher energy density and all-weather capability (Choupin et al., 2022). Based on Zhang et al. (2018), it is estimated that the theoretical global resource of wave energy is 2 TW. Wave energy devices have been developed in five main forms, such as oscillating water column, overtopping, point-absorber, bottom-articulated, and multi-body articulated (Zhang et al., 2019). Point-absorber WECs have gained much attention in the academic due to their high energy conversion efficiency, low construction and installation costs, low impact on marine environment, and flexible layouts.

To improve the conversion of wave energy, combining multiple point-absorber WECs into a wave farm is a common approach. Meanwhile, a bottom-mooring platform or an offshore floating wind turbine can be the carrier of the WEC array, which can make the WECs more cost-effective, reliable, and stable (Li and Yu, 2012; Nguyen et al., 2020). Zhang et al. (2016) developed a novel wave energy conversion means through integrating a buoy array with a flexible runway. They evaluated the influence of the PTO properties and wave parameters on the runway displacement and the power capture performance of the buoy array. Chandrasekaran and Sricharan (2021) proposed three multi-body floating WEC systems with different layouts, which all consisted of a tension-legged cylinder and multiple point-absorber WECs. They utilized WEC-Sim to investigate the impact of the number of WEC floats on the system's overall performance. Ghafari et al. (2022) explored the effects of WEC diameter and number on the dynamic behavior of an integrated system that combines a semi-submersible wind turbine platform with an array of Wavestar WEC. The results showed that hydrodynamic interactions reduced the energy conversion of the WEC array, especially at small wave frequencies. Zhou et al. (2023) presented a hybrid design that integrated a heaving WEC onto a Spar-type floating wind turbine. The results implied that the incorporation of the WEC did not significantly detrimentally affect the motion performance of the platform, and even improved its rotational stability. Zhu et al. (2023) investigated an integrated system with a point-absorber WEC array and a semi-submersible platform. They analyzed the influence of the WEC parameters, wave parameters, and

* Corresponding author.
E-mail address: zhiming.yuan@strath.ac.uk (Z. Yuan).

https://doi.org/10.1016/j.oceaneng.2024.119548
Received 27 August 2024; Received in revised form 4 October 2024; Accepted 16 October 2024
Available online 21 October 2024

submergence of the base column on the platform response and the energy conversion of the WEC array. Wu et al. (2024) evaluated the influence of the shape of point-absorber WEC on the performance of a wind-wave integrated system. It was found that the integrated system with truncated conical WECs was superior to cylindrical and conical ones in terms of power output. In addition, the platform motion was not conducive to the power conversion of the WEC array. Zhang et al. (2023) conceptualized a novel wind-wave energy integration, and explored its dynamic behavior with various numbers of WECs. They found that with an increase in the number of WECs, the platform response and the absorbed power of the WEC array increased. Jin et al. (2023) performed an optimization and evaluation analysis of an integrated system composed of an oscillating-body WEC array and a semi-submersible wind turbine. The results reflected that the presence of the WEC array did not adversely affect the stability of the platform system. In addition, the WEC array could reduce the fluctuation in the mooring tension response. Wei et al. (2024) proposed a wind-wave energy hybrid system based on the Jacket platform, and analyzed the power capture performance of a point-absorber WEC array. The results indicated that the capture width ratio of WEC array could be more than 0.5 as the wave period was close to the natural period, and the capture width ratio of individual WEC may be larger than 0.8. Rony and Karmakar (2024) presented a wind-wave energy integrated system including a TLP and a heaving oscillating WEC array, and analyzed the effects of the WEC array on the power capture performance of wind turbine.

In fact, real ocean waves are mostly short-crested, and they propagate along multiple directions. Many scholars have investigated the effects of wave directionality on various offshore structures. Sørum et al. (2019) predicted the fatigue damage of bottom-fixed wind turbine under different wave parameters. It was found that for hydrodynamically sensitive base structures, their fatigue damage increased up to 80% under short-crested waves, compared to long-crested waves. Viuff et al. (2019) evaluated the impact of wave directionality on the extreme response of a simplified end-anchored pontoon bridge, including the transverse and vertical displacement response spectra of the cross-section, as well as the ultimate Von Mises stresses. Jiao et al. (2019) utilized an experimental study to identify the differences in ship motion and load response under short-crested and long-crested wave conditions. Meanwhile, through numerical sea-keeping simulations, they evaluated the impact of the spreading exponent on ship motions and wave loads under short-crested waves. Ji et al. (2015) investigated the influence of wave directionality on the wave run-ups and forces of a vertically fixed cylindrical array under short-crested waves. The results showed that the multi-directional wave run-up was larger than that of the unidirectional one, and the maximum transverse force appeared at the rear cylinder. Li and Liu (2022) analyzed the dynamic response of a semi-submersible floating wind turbine under short-crested waves. The results showed that compared to long-crested waves, the structural integrity was better under short-crested waves. Zhang et al. (2021) adopted the URANS method to investigate the speed loss and water-jet performance of a water-jet propelled trimaran under short-crested wave conditions. They found that under short-crested waves, the variation of the heave and pitch oscillations of the trimaran brought about an added resistance that caused the speed loss as well as the degradation of water-jet performance. Deng et al. (2022) numerically simulated the hydroelastic and vortex-induced vibrations of a two-tube submerged floating tunnel under short-crested waves. The results implied that the short-crested waves amplified the response of the floating tunnel in the transverse and vertical directions through the excitation of the eigenmodes. Lee et al. (2024) predicted the added resistance of the KCS hull under both short-crested and long-crested waves by using the spectral method. In addition to this, they also compared the motion RAO and flow field characteristics under these two wave conditions. Göteman et al. (2018) compared the energy conversion of a point-absorber WEC array under long-crested and short-crested waves with an analytical approach. The results showed that the performance of the WEC array under short-crested waves was not inferior to that under long-crested ones, and the power absorption process was more stable. Ning et al. (2024) investigated the hydrodynamic performance of a semi-submersible wind turbine platform under short-crested and long-crested waves. It was found that the wave-structure interaction characteristics could be altered by the wave distribution, which needed to be carefully considered in practical engineering applications. The above studies suggest that short-crested waves may significantly affect the dynamic response and hydrodynamic forces of offshore structures. However, to the authors' knowledge, few studies have addressed the effects of wave distribution on power capture platforms. Therefore, this paper investigates the dynamic behavior of a novel floating power capture platform under different wave distributions. In order to simulate short-crested waves, the JONSWAP spectrum is modified into a three-dimensional wave spectrum using a spreading function, which ensures that the total wave energy remains constant. The platform motion, mooring line tension, and power captured performance of the WEC array are investigated in the current study. By comparing the results under different spreading exponents, the influence of wave directionality on the power capture platform can be evaluated.

Section 2 presents the motion equation in the time domain of a multi-body floating connected system, the mathematical model of short-crested waves, the formula of the wave excitation forces, and the power capture equation of a WEC. Section 3 gives the characteristics of the semi-submersible platform, mooring system and point-absorber WEC, as well as a schematic diagram of the power capture platform. In order to ensure the reliability of the numerical analysis, Section 4 presents the mesh convergence analysis and hydrodynamic validation of the platform and WEC models. The results and discussions of the present study are demonstrated in Section 5. Lastly, Section 6 summarizes some important conclusions.

2. Theoretical background

2.1. Time-domain simulation of a multi-body floating connected system

Due to the articulated devices in a multi-body floating connection system, the displacement continuity condition should be considered in its time-domain motion equation,

$$\begin{cases} [[\boldsymbol{M}+\boldsymbol{A}(\infty)]]_{6N\times 6N}[\ddot{\boldsymbol{x}}(t)]_{6N\times 1}+\left[\int_0^t \boldsymbol{R}(t-\tau)\dot{\boldsymbol{x}}(\tau)d\tau\right]_{6N\times 1}+[\boldsymbol{C_v}+\boldsymbol{C_{PTO}}]_{6N\times 6N}[\dot{\boldsymbol{x}}(t)]_{6N\times 1}+ \\ [\boldsymbol{K_h}+\boldsymbol{K_{PTO}}]_{6N\times 6N}[\boldsymbol{x}(t)]_{6N\times 1}+[\boldsymbol{H}]^T_{6N\times m}[\boldsymbol{F_c}(t)]_{m\times 1}=[\boldsymbol{F_{ex}}(t)]_{6N\times 1}+[\boldsymbol{F_m}(t)]_{6N\times 1} \\ [\boldsymbol{H}]_{m\times 6N}[\boldsymbol{x}(t)]_{6N\times 1}=[\boldsymbol{0}]_{m\times 1} \end{cases} \tag{1}$$

where $\boldsymbol{M}$ and $\boldsymbol{A}(\infty)$ are the mass and added mass matrix at infinite frequency, respectively; $\boldsymbol{R}(t)$ is the retardation matrix, which represents the fluid memory effects; $\boldsymbol{C_v}$ and $\boldsymbol{C_{PTO}}$ refer to the linearized viscous damping and power take-of (PTO) damping matrices, respectively; $\boldsymbol{K_h}$

and $\boldsymbol{K_{PTO}}$ are the hydrostatic stiffness and PTO stiffness matrices, respectively; $\boldsymbol{F_{ex}}(t)$ is the wave excitation force; $\boldsymbol{F_m}(t)$ is the mooring force, which can be solved by the lumped mass method (Hall and Goupee, 2015); $\boldsymbol{F_c}(t)$ is the connecting force on the hinge device, and $\boldsymbol{H}$ refers to the constraint matrix (Zhao et al., 2023); N and m denote the numbers of floating bodies and degrees of freedom constrained in the system, respectively.

2.2. Modelling of short-crested waves

In the real ocean environment, most waves are actually short-crested, and they propagate along multiple directions. Therefore, a wave spectrum that takes into account both frequency and direction is used to model the short-crested wave,

$$S(\omega,\theta)=D(\theta)\bullet S(\omega) \tag{2}$$

where $S(\omega)$ refers to the JONSWAP spectrum, and $D(\theta)$ represents the directionality function (Barltrop, 1998). They can be expressed respectively as:

$$S(\omega)=\alpha H_s^2\frac{\omega^{-5}}{\omega_p^{-4}}exp\left[-1.25\left(\omega/\omega_p\right)^{-4}\right]\gamma^{exp\left[-\frac{\left(\omega-\omega_p\right)^2}{2\sigma^2\omega_p^2}\right]} \tag{3}$$

$$D(\theta)=C\bullet\cos^n(\theta-\overline{\theta}),for-\frac{\pi}{2}\le\theta-\overline{\theta}\le\frac{\pi}{2} \tag{4}$$

where α is the spectral parameter; H_s, ω_p and γ are the significant wave height, spectral peak period and enhancement factor, respectively; As $\omega<\omega_p$, the spectral parameter σ is equal to 0.07, while it is taken as 0.09 for $\omega<\omega_p$; n is the spreading exponent; $\overline{\theta}$ is the dominant wave direction; and the value of C needs to satisfy a condition,

$$\int_{-\frac{\pi}{2}+\overline{\theta}}^{\frac{\pi}{2}+\overline{\theta}}S(\omega,\theta)d\theta=S(\omega) \tag{5}$$

Based on this condition, the above equation can be changed into:

$$\int_{-\frac{\pi}{2}}^{\frac{\pi}{2}}D(\theta)d\theta=C\int_{-\frac{\pi}{2}}^{\frac{\pi}{2}}cos^n\theta d\theta=1 \tag{6}$$

Fig. 1 presents the directionality functions for $n=2-8$. From the figure, it can be observed that as $n=2$, the wave exhibits a broadband distribution in direction. It is also found that the wave directional distribution becomes narrow as the spreading exponent increases.

For the short-crested irregular wave, the wave elevation can be expressed as (Faltinsen, 1993):

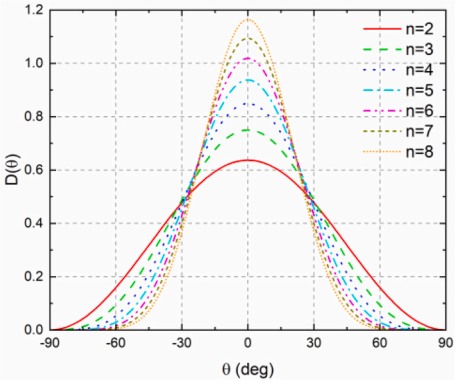

Fig. 1. Spreading functions with various spreading exponents.

$$\xi(x,y,t)=\sum_{l=1}^{L}\sum_{g=1}^{G}a_{lg}\cos\left(\omega_l t+\varepsilon_{lg}-k_l x\cos\theta_g-k_l y\sin\theta_g\right) \tag{7}$$

where $a_{lg}=\sqrt{2S(\omega_l,\theta_g)\Delta\omega\Delta\theta}$, k_l and ε_{lg} are the wave amplitude, wave number and random phase of a wave component with frequency ω_l and direction θ_g, respectively; L and G denote the numbers of wave components and directions, respectively.

2.3. Wave excitation forces

Three-dimensional potential flow theory and BEM are adopted to solve the first- and second-order velocity potentials (Li et al., 2023). First- and second-order wave force transfer functions are then calculated by the direct integration over the wet body surface. Based on the wave elevations and transfer functions, the corresponding time series of the wave excitation forces can be obtained. For short-crested wave, the first-order and second-order wave forces exerted on the body can be expressed as, respectively (Molin, 2022):

$$F_{ex}^{(1)}(t)=\sum_{l=1}^{L}\sum_{g=1}^{G}a_{lg}Q^{(1)}\left(\omega_l,\theta_g\right)cos\left(\omega_l t+\varepsilon_{lg}+\beta^{(1)}\left(\omega_l,\theta_g\right)\right) \tag{8}$$

$$F_{ex}^{(2)}(t)=\sum_{l=1}^{L}\sum_{k=1}^{L}\sum_{g=1}^{G}\sum_{r=1}^{G}a_{lg}a_{kr}\left[Q_{Re}^{(2)}\left(\omega_l,\omega_k,\theta_g,\theta_r\right)cos\left(\left(\omega_l-\omega_k\right)t+\left(\varepsilon_{lg}-\varepsilon_{kr}\right)\right)+Q_{Im}^{(2)}\left(\omega_l,\omega_k,\theta_g,\theta_r\right)sin\left(\left(\omega_l-\omega_k\right)t+\left(\varepsilon_{lg}-\varepsilon_{kr}\right)\right)\right] \tag{9}$$

where $Q^{(1)}$ and $\beta^{(1)}$ refer to the amplitude and phase of the linear wave force transfer function, respectively; $Q_{Re}^{(2)}$ and $Q_{Im}^{(2)}$ denote the real and imaginary components of the difference-frequency quadratic transfer function, respectively.

In order to improve computational efficiency, the Newman approximation is utilized to solve the second-order difference-frequency forces (Newman, 1974). The core of this method is to approximate the non-diagonal values with the diagonal values in the quadratic transfer function matrix,

$$Q_{Re}^{(2)}\left(\omega_l,\omega_k,\theta_g,\theta_r\right)=\frac{1}{2}\left[Q_{Re}^{(2)}\left(\omega_l,\omega_l,\theta_g,\theta_r\right)+Q_{Re}^{(2)}\left(\omega_k,\omega_k,\theta_r,\theta_g\right)\right] \tag{10}$$

$$Q_{Im}^{(2)}\left(\omega_l,\omega_k,\theta_g,\theta_r\right)=\frac{1}{2}\left[Q_{Im}^{(2)}\left(\omega_l,\omega_l,\theta_g,\theta_r\right)-Q_{Im}^{(2)}\left(\omega_k,\omega_k,\theta_r,\theta_g\right)\right] \tag{11}$$

2.4. Power capture equation of the PTO system

Fig. 2 shows the illustration of the WEC with the PTO system. Based on Ghafari et al. (2021), a hinged point with rotational damping is utilized to simulate the PTO system, so the torque τ_{PTO} acting on the WEC can be formulated as:

$$\tau_{PTO}=-B_P\dot{\theta} \tag{12}$$

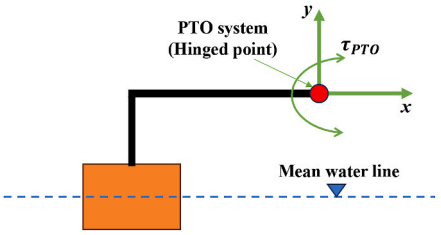

Fig. 2. Illustration of the WEC with the PTO system.

where $\dot{\theta}$ is the angular velocity of the WEC; B_P is the rotational damping of the PTO system.

Therefore, the instantaneous absorbed power of the WEC can be expressed as:

$$P_I = |\tau_{PTO}\dot{\theta}| = B_{PTO}\dot{\theta}^2 \tag{13}$$

Then, the mean absorbed power of the WEC during the interval of T is,

$$P_M = \frac{1}{T}\int_t^{t+T} P_I dt = \frac{1}{T}\int_t^{t+T} B_{PTO}\dot{\theta}^2 dt \tag{14}$$

In the present study, multiple WECs are integrated with the floating platform. Based on the operation principle of the WEC above, its mean absorbed power among the power capture platform can be derived as:

$$P'_M = \frac{1}{T}\int_t^{t+T} B_P\left(\dot{\theta}_p - \dot{\theta}_w\right)^2 dt \tag{15}$$

where $\dot{\theta}_p$ and $\dot{\theta}_w$ are the angular velocities about the hinged point of the platform and the WEC, respectively.

3. Characteristics of the floating power capture platform

This paper proposed a novel energy capture platform concept that combines a point-absorber WEC array with a semi-submersible platform.

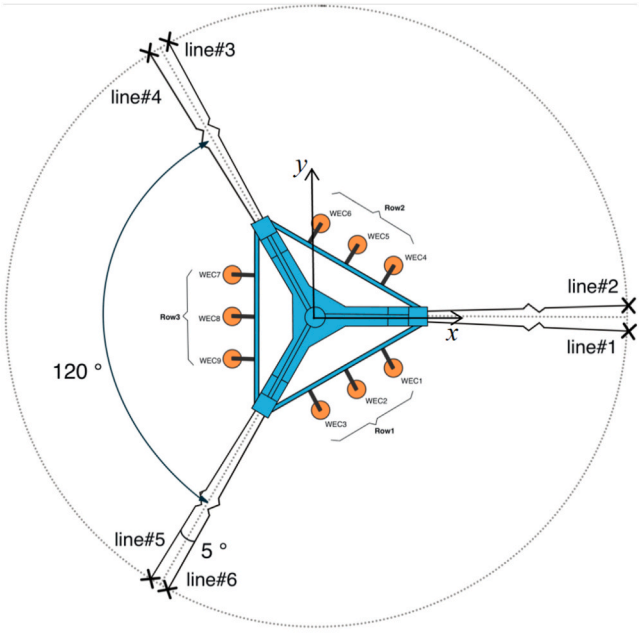

(a) Top view

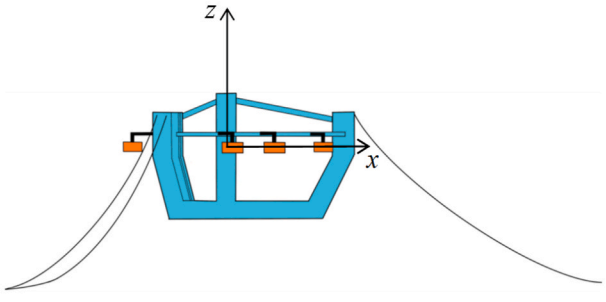

(b) Side view

Fig. 3. A schematic diagram of the floating power capture platform.

Table 1
Main properties of the platform, mooring system and WEC.

	Property	Value
Platform	Draft/(m)	30
	Displacement/(kg)	1.64E7
	Mass/(kg)	1.61E7
	Center of gravity (COG) below MWL (Mean sea level)/(m)	9.68
	Radius of gyration around *x*-axis/(m)	37
	Radius of gyration around *y*-axis/(m)	37
	Radius of gyration around *z*-axis/(m)	20
Mooring	Number of mooring lines	6
	Outer diameter of mooring line/(mm)	120
	Length of mooring line/(m)	800
	Axial stiffness/(kN)	1.243E6
	Mass in water/(kg/m)	303
	Radius from platform center to fairleads/(m)	54.5
	Radius from platform center to anchors/(m)	830
	Fairlead position above MWL/(m)	15
	Anchor position below MWL/(m)	60
WEC	Radius/(m)	4.402
	Draft/(m)	2.201
	Elevation above MSL/(m)	2.201
	Elevation of hinge point above MSL/(m)	5.987
	Horizontal distance of hinge point from COG/(m)	10.696
	Mass/(kg)	1.484E5
	COG below MSL/(m)	0
	Roll inertia/(kg • m^2)	1.097 E+06
	Pitch inertia/(kg • m^2)	1.540 E+06
	Yaw inertia/(kg • m^2)	1.701 E+06

The semi-submersible platform is composed of a center column, three inclined cross-braces, three partially-inclined side columns, and a submerged pontoon, of which the mooring system consists of three sets of catenary chains. In order to arrange the WEC array symmetrically into the platform, three horizontal cross braces are set between three side columns. A schematic diagram of the power capture platform is presented in Fig. 3, while Table 1 lists the main parameters of the platform, mooring system and WEC. Notably, the numbering of the individual WEC and WEC row among the WEC array is given in Fig. 3.

Based on the motion and energy conversion mode of the power capture platform, it's better to derive the detailed composition forms of the physical quantities K_{PTO}, C_{PTO}, and H in Eq. (1). However, since the present study does not consider the PTO stiffness, only the latter two quantities need to be provided. Therefore, the detailed PTO damping and constraint matric are presented in Appendix A. Meanwhile, the calculation equation of the captured power is also presented.

4. Validation of the numerical models

In the present study, the dynamic response of the power capture platform is mainly investigated by numerical means. Therefore, to ensure the reliability of the following numerical analysis, it is necessary to conduct the hydrodynamic validation of the point-absorber WEC and semi-submersible platform.

4.1. Mesh convergence analysis

Prior to the validation of the point-absorber WEC and semi-submersible platform, it is necessary to conduct the mesh convergence analysis of their numerical models. In the present study, the surfaces of the platform and WEC are divided into 14000 and 2640 panel elements, respectively. There are two methods for calculation of the steady drift forces, namely the far-field method and near-field method. By comparing the results under these two methods, the mesh convergence can be verified (Yue et al., 2020). Fig. 4 illustrates the surge steady drift forces of the platform and WEC under unit wave amplitude with these two methods. As shown in the figure, the results agree well, which

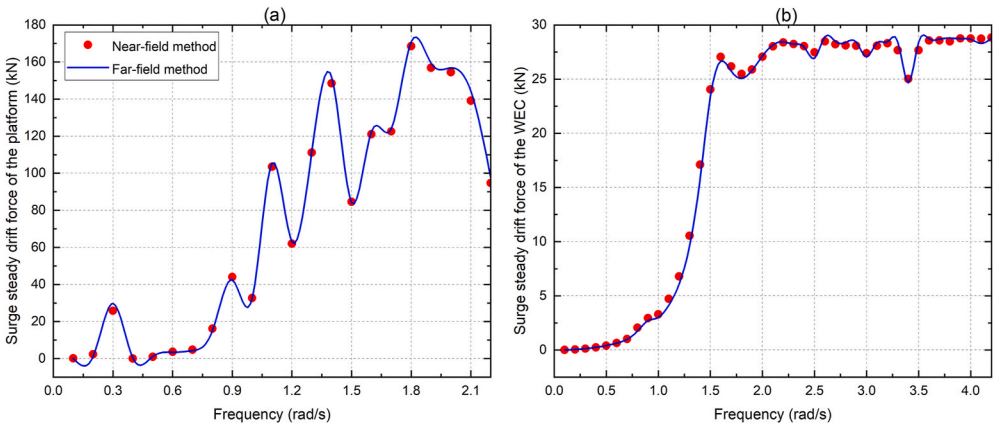

Fig. 4. Comparison of the surge steady drift forces of the platform (a), and WEC (b) with near-field and far-field methods.

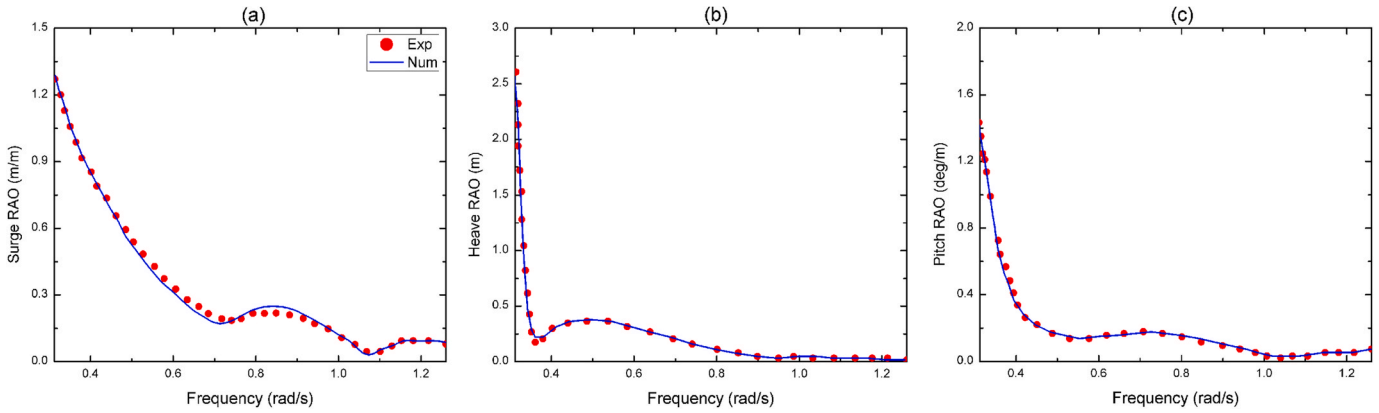

Fig. 5. Comparison of the platform surge (a), heave (b) and pitch (c) RAOs between the experimental and numerical results.

indicates that their numerical models satisfy the accuracy requirements.

4.2. Semi-submersible platform model

The semi-submersible platform was designed by Shanghai Jiao Tong University (Cao et al., 2021). Cao et al. obtained the damping ratios of the platform in six degrees of freedom (DOFs) through free decay tests. In the present study, the viscous damping of the platform model is considered based on the damping ratios. Fig. 5 compares the response amplitude operators (RAOs) of the platform under experimental and numerical studies for the surge, heave and pitch DOFs. From the figure, it can be observed that the numerical results are in good agreement with the experimental data, which ensures the reliability of the platform model.

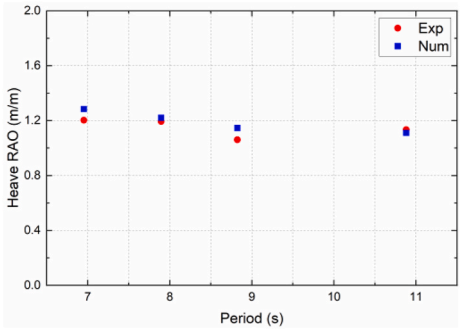

Fig. 6. Comparison of the heave RAOs of point-absorber WEC between the numerical and experimental results.

4.3. Point-absorber WEC model

The prototype of this point-absorber WEC was proposed by He et al. (2023). In their work, the heave RAOs of the WEC floater were tested at four specific frequencies. The WEC model is developed and simulated in the frequency domain based on the properties in Table 1. As illustrated by Zhou et al. (2020), the damping correction to the WEC is negligible when its diameter-to-draft ratio is large. Since the diameter-to-draft ratio of the WEC in the present study is large enough, the impact of viscous damping is not considered. Meanwhile, it is assumed that there is no PTO damping at the hinge point. Fig. 6 shows the heave RAOs of WEC at the corresponding wave frequencies from both experimental and numerical studies. As seen in the figure, the numerical results agree with the experimental data well, which implies that the WEC model is reliable.

5. Results and discussion

This section focuses on the dynamic behavior of the power capture platform under short-crested wave conditions. The operating site is

Table 2
Five load cases.

	H_s	T_p	γ
LC1	2.0	6.2	2.0
LC2	3.8	8.3	2.4
LC3	6.8	10.1	3.7
LC4	8.1	11.4	3.1
LC5	10.3	14.1	2.0

located 20 km offshore in the north of the South China Sea (Cao et al., 2023). Therefore, five load cases (LCs) are selected to study the dynamic response of the platform and the power capture performance of the WEC array, as shown in Table 2. It is assumed that the wave incidence angle is zero degree, and there is no influence of wind and current. LC1-LC3 are operational conditions, while LC4-LC5 are extreme conditions. When the power capture platform is under operational conditions, the WEC array can work normally. However, under extreme conditions, to avoid damage to the WECs, they have to be locked and remain relatively stationary with the platform.

5.1. Characteristics of short-crested wave conditions

To characterize the short-crested waves, this section introduces the three-dimensional wave spectra of LC2 for various spreading exponents, as shown in Fig. 7. As demonstrated in the figure, the spectral value of the wave spectrum is maximal at the spectral peak frequency. In addition, it can be inferred that a larger spreading component indicates less energy is focused around the peripheral direction, and more around the dominant direction. Furthermore, since the total energy of the wave spectrum remains constant, the spectral value around the dominant direction increases as the spreading exponent becomes larger.

5.2. PTO damping coefficients

In order to determine the optimal PTO coefficients for the point-absorber WEC under three operational LCs, this section presents a sensitivity analysis of its power capture performance. Based on the layout of the WEC array and the wave incidence angle, WEC-1 and WEC-2 are defined to represent the study objects, respectively. WEC-1 refers to the WECs among Row 3, while WEC-2 stands for the WECs among Rows 1 or 2. Figs. 8 and 9 present the results of WEC-1 and WEC-2 with various PTO damping coefficients, respectively, for the absorbed power under short-crested wave conditions. From Fig. 8, it can be observed that under LC1-LC3, WEC-1 absorbs the most power at the PTO damping coefficients of 2.5E4 kN • m • s/rad, 4.6E4 kN • m • s/rad and 6.7E4 kN • m • s/rad, respectively. In addition, it can be found in the figure that under LC1, the variation pattern of the absorbed power of WEC-1 regarding the spreading component is different from that of the other two LCs. Under LC1, the absorbed power of WEC-1 regarding the spreading component shows a decreasing trend as a whole, but it increases with an increase in the spreading component under the other two LCs. The above phenomenon indicates that the vertical motion of WEC-1 excited by LC1 is larger when the wave directionality is relatively scattered, while under LC2 and LC3, the situation is opposite. From Fig. 9, it can be seen that under LC1-LC3, the absorbed power of WEC-2 reaches maximal at the PTO coefficients of 2.5E4 kN • m • s/ rad, 4.4E4 kN • m • s/rad and 6.7E4 kN • m • s/rad, respectively. In addition, the absorbed power of WEC-2 has a decreasing trend about the spreading component. This is because WEC-2 under a short-crested wave with a relatively scattered distribution can be excited with a more pronounced vertical motion due to the angle with the incidence direction. It is noteworthy that under the identical LC, WEC-2 absorbs significantly more power than WEC-1, which accounts for the fact that the rotational motion of the hinge device increases due to the layout of WEC-2.

Therefore, the PTO damping coefficients of WECs among Rows 1 or 2 under LC1-LC3 are set as 2.5E4 kN • m • s/rad, 4.4E4 kN • m • s/rad and 6.7E4 kN • m • s/rad in the following study, respectively. Meanwhile, 2.5E4 kN • m • s/rad, 4.6E4 kN • m • s/rad and 6.7E4 kN • m • s/rad are the PTO damping coefficients of WECs among Row3, respectively.

5.3. Platform motion response

To analyze the dynamic response of the platform under short-crested wave conditions, the mean response and standard deviation (STD) of the surge, heave, and pitch motions are presented in this section, as shown in Figs. 10–12. From Fig. 10(a), it can be observed that under LC1, the variation of the surge mean response regarding the spreading exponent is slight, which implies that the wave directionality distribution hardly affects the equilibrium position of the platform in the surge direction. However, as $n = 2$, the surge response has a smaller STD compared to a larger spreading component, which may be due to the fact that for $n = 2$, the scattered wave distribution is unable to stimulate a larger motion in the surge direction of the platform. From Fig. 10(b)-10(e), it can be noticed that under LC2-LC5, the surge mean response shows an increasing trend about the spreading component, which indicates that the mean drift force exerted on the platform increases with the focus of the wave distribution. In addition, under LC5, the variation pattern of the surge STD about the spreading component is different from that under LC2-LC4. Under LC2-LC4, the short-crested waves with more focused energy can excite a larger surge slow-drift force, which leads to a more intense surge response of the platform. As a result, the surge STD has an increasing trend about the spreading component. However, under LC5, the surge STD decreases as the spreading component increases. This may be attributed to the fact that the performance of the mooring system exceeds the excitation impact of the slow-drift force. From Fig. 11(a), it can be observed that there is an obvious jump from $n = 3$ to $n = 4$ in the mean response of the platform's heave motion under LC1, and it remains constant when $n < 4$ or $n > 3$. This indicates that as the spreading component exceeds a certain threshold, the constraint force at the articulation simulates the platform upward from its vertically equilibrium position. In addition, the heave STD increases as the spreading exponent increases. This is due to the fact that the short-crested waves with more focused energy excites a larger heave motion. From Fig. 11(b), it can be found that under LC2, the mean value and STD of the heave response for $n = 2$ are similar to those for $n = 8$, but smaller than those for $n = 3 - 7$. This demonstrates that the platform is excited with a smaller heave response when the wave distribution is significantly scattered or focused. From Fig. 11(c)-11(e), it can be seen that under LC3-LC5, the variation patterns of the heave mean

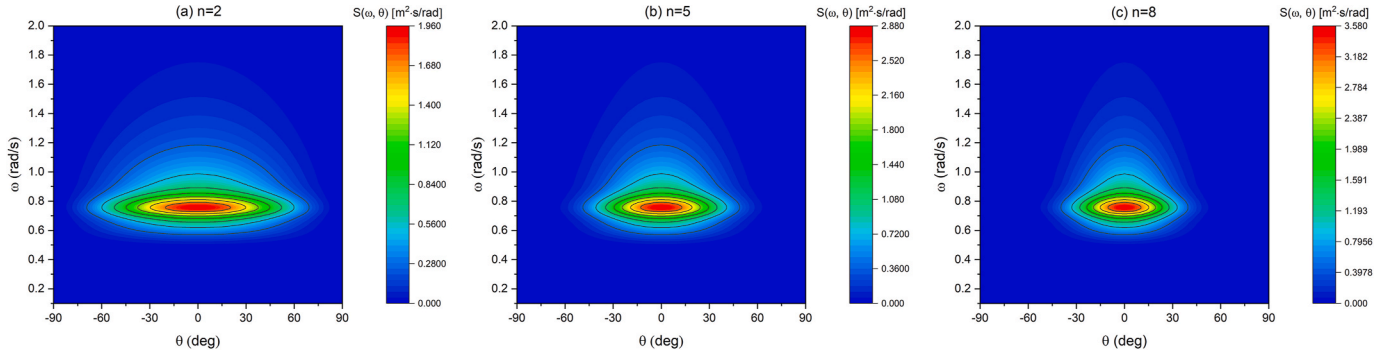

Fig. 7. Three-dimensional wave spectra of LC2 with various n.

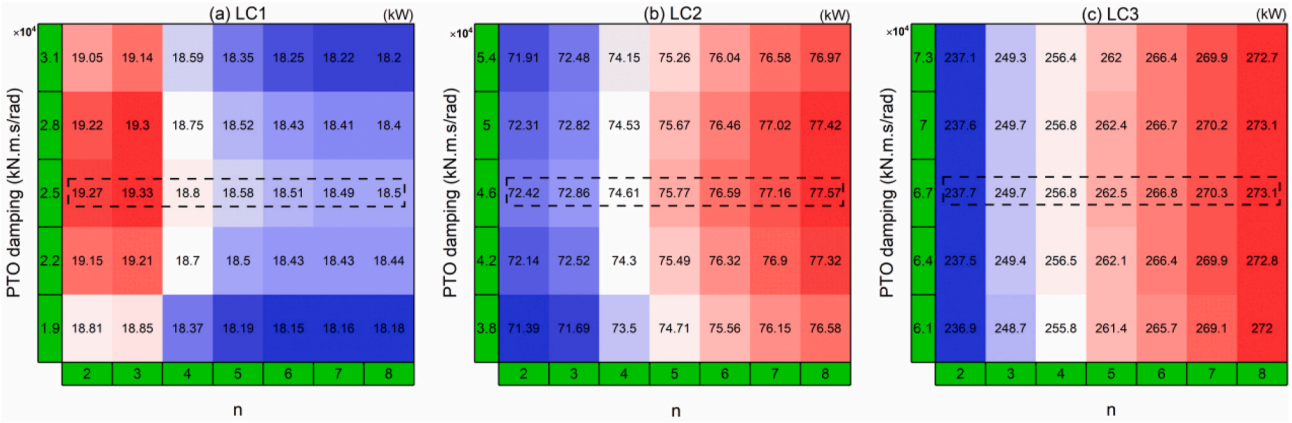

Fig. 8. Absorbed power of WEC-1 for various n versus different PTO damping coefficients under three operational LCs.

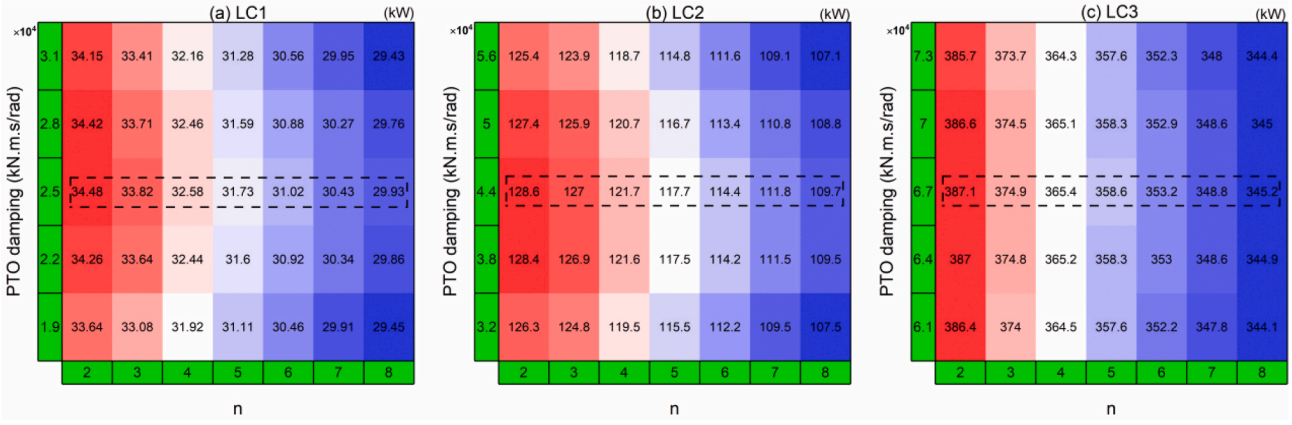

Fig. 9. Absorbed power of WEC-2 for various n versus different PTO damping coefficients under three operational LCs.

response or STD regarding the spreading component are similar. For the mean value, it remains almost constant for different spreading components. This means that the short-crested waves do not change the platform equilibrium position in the heave direction through the constraint forces at the articulation. As for the STD, it has an upward trend about the spreading component, which is due to the fact that the more focused the wave distribution is, the more intense the heave response is. It is worth noting that the variation pattern of the pitch STD about the spreading component under LC1 is similar to that of the surge response, as shown in Fig. 12(a). This phenomenon is attributed to the coupling effects between the surge and pitch motions. In addition, the variation trends of the pitch mean response under LC1, and the pitch mean response and STD regarding the spreading component under LC2-LC5 are similar to those of the heave response. This indicates that the coupling effects between the heave and pitch motions are significant.

5.4. Mooring line tension

To analyze the dynamic response of the mooring line under short-crested wave conditions, Fig. 13 shows the maximum value, mean value, and STD of the #5 tension response. The reason for selecting #5 as the object is that its tension response is maximal under this wave incidence direction, which is crucial for assessing the safety and reliability of the mooring system. From Fig. 13(a)-13(c), it can be observed that under LC1-LC3, the tension mean response remains almost constant regarding the spreading component. This is due to the fact that although the longitudinal equilibrium position of the platform varies for different spreading components, it is not able to make a significant change in the average suspended length of #5 in the water. For the STD of tension response, it can be found in Fig. 13(a) that it is maximal for $n = 3$ and minimum for $n = 8$. This implies that the of oscillation in the tension response is more intense as the wave directionality is relatively scattered. However, a different situation occurs in Fig. 13(b), which is that the tension STD reaches maximal for $n = 8$. This indicates that under LC2, the tension can be excited with a more intense response under a short-crested wave with more focused energy. From Fig. 13(c), it can be seen that there is a decreasing trend in the tension STD from $n = 5$ to $n = 8$ under LC3. This reflects that the more focused the wave directionality is, the weaker the tension oscillation is. In Fig. 13(d)-13(e), it can be inferred that under LC4-LC5, the mean value and STD of the tension response show an overall decreasing trend about the spreading component, which indicates that the short-crested wave with more scattered energy can stimulate a more pronounced tension response. It is noteworthy that the tension response for $n = 3$ is larger than that for $n = 2$ under LC4. This may be due to the fact that the wave distribution with $n = 3$ is more conducive to the excitation of the tension response. In addition, for the maximum tension, it can be noticed that its variation pattern under LC1-LC5 regarding the spreading exponent is different from those of the mean response and STD, and relatively complicated. This is attributed to the fact that the dynamic response under the irregular wave conditions has an obvious randomness. Furthermore, it can be inferred that under LC1-LC3, the difference between the maximum tension for different spreading components is slight, while the situation is opposite under LC4-LC5. For different spreading components, the maximum value of the maximum tension response is about 30% larger than the minimum value under LC4-LC5. This reflects that the wave directionality is closely related to the safety and reliability of the mooring system under extreme conditions. It is recommended that

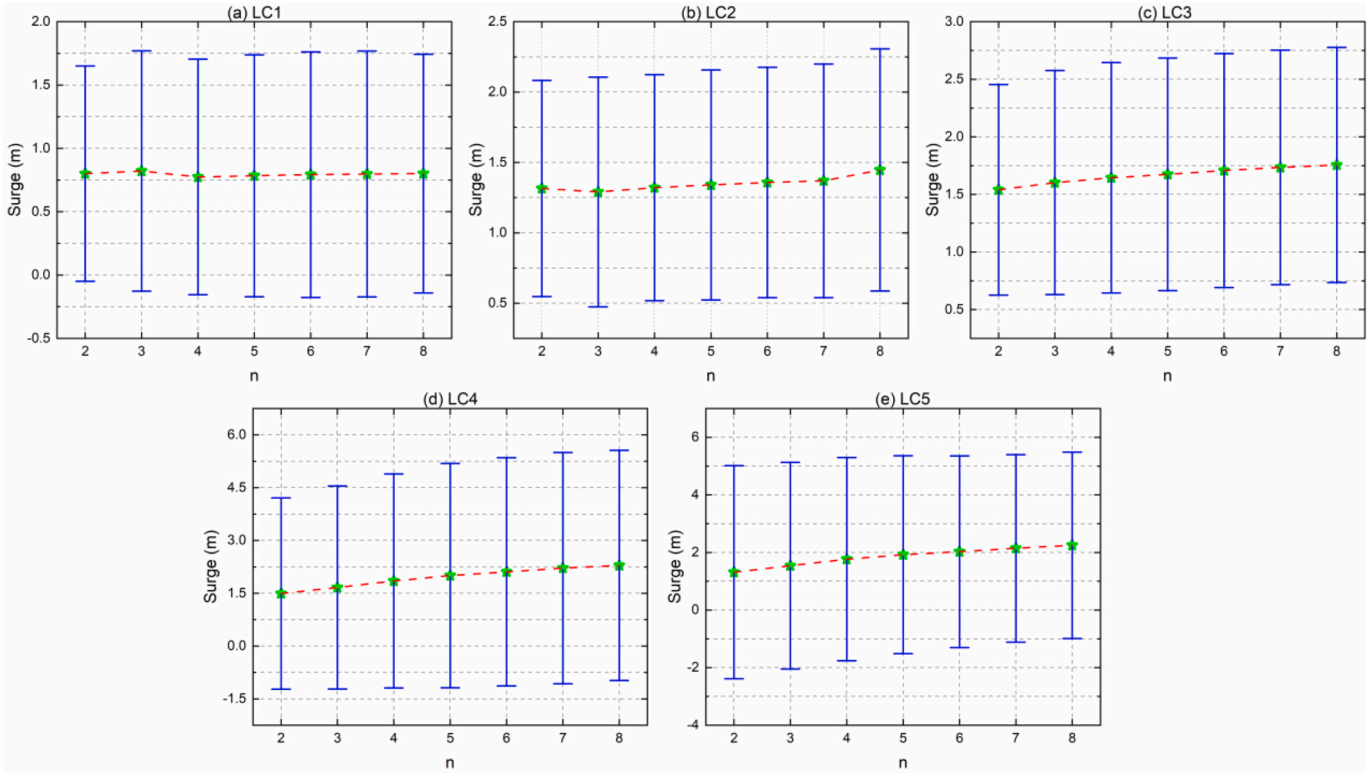

Fig. 10. Surge mean response and STD of the platform for various *n* under five LCs.

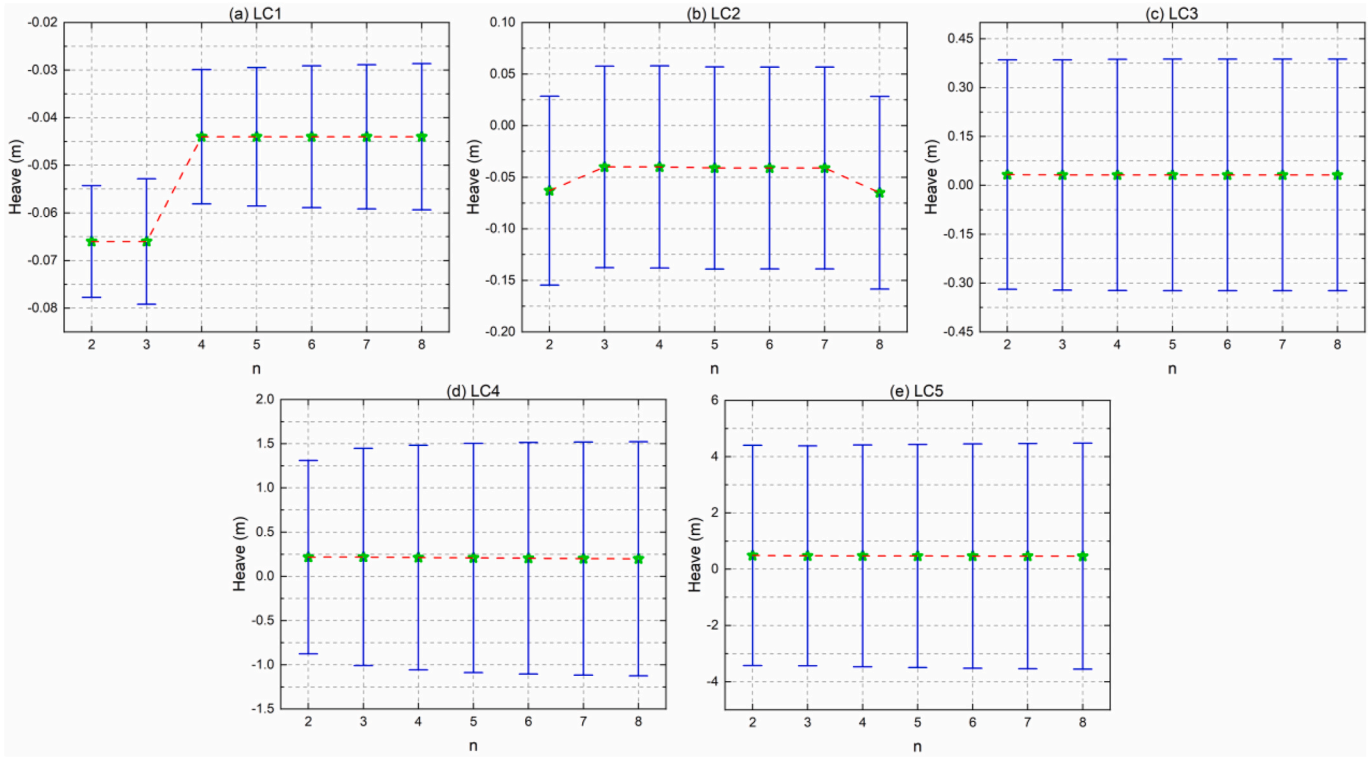

Fig. 11. Heave mean response and STD of the platform for various *n* under five LCs.

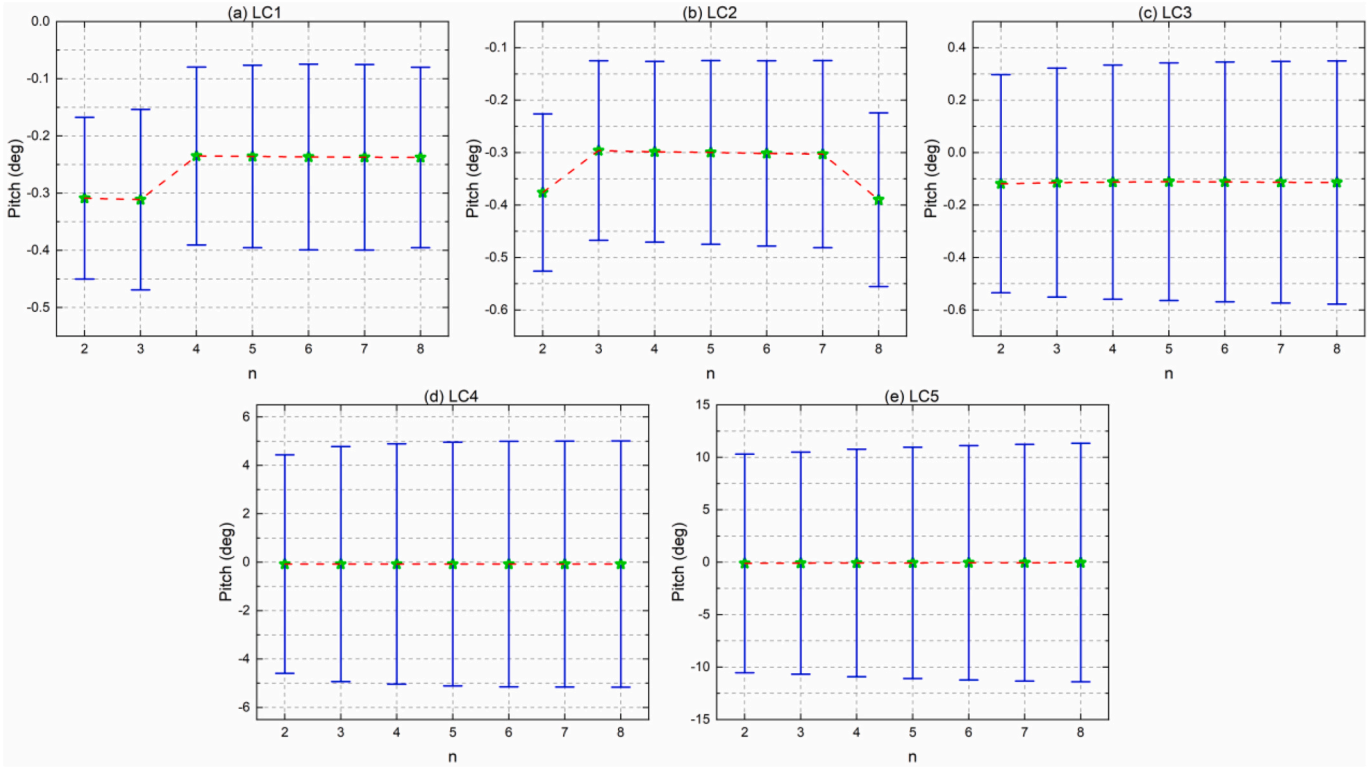

Fig. 12. Pitch mean response and STD of the platform for various *n* under five LCs.

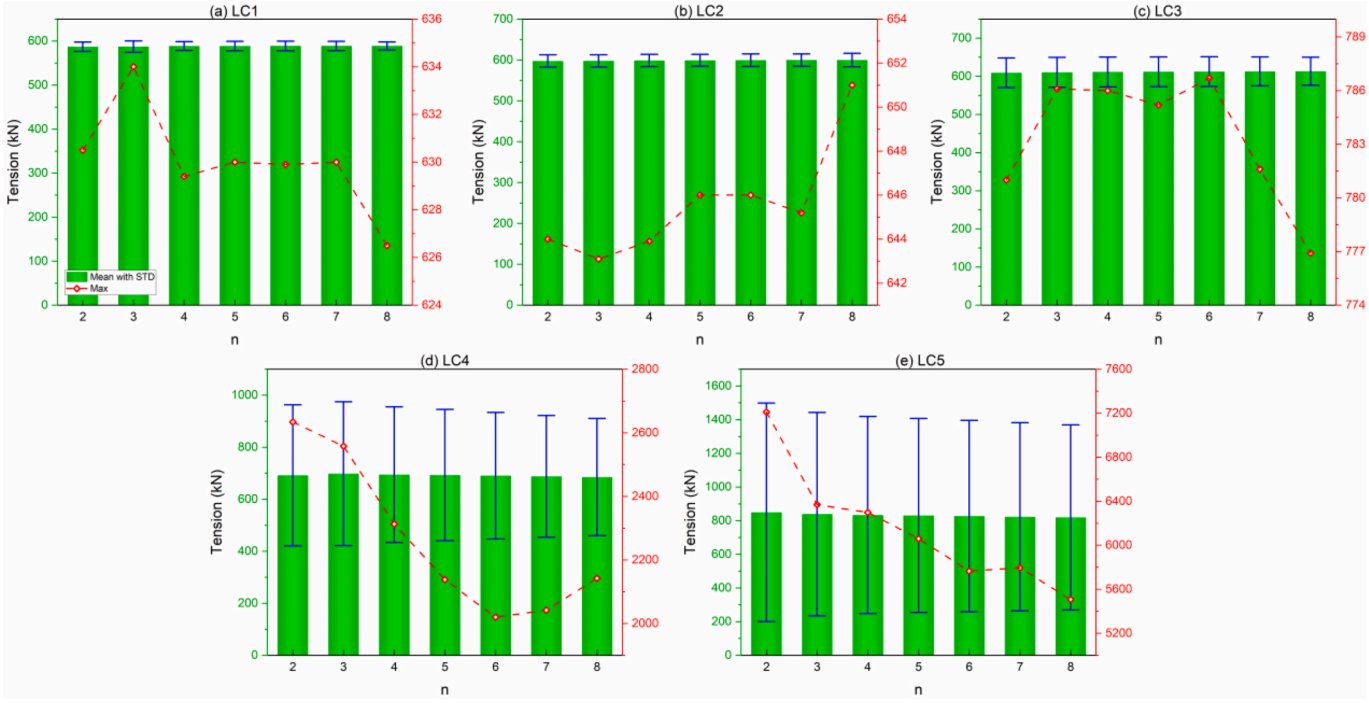

Fig. 13. The maximum response, mean and STD values of #5 tension for various *n* under five LCs.

the wave directionality should be determined in advance for the design of mooring systems.

5.5. Power capture performance

To investigate the power capture performance of point-absorber WECs under short-crested wave conditions, this section analyzes the power absorption of the individual WEC, WEC row, and WEC array in Sections 5.5.1, 5.5.2 and 5.5.3, respectively. In addition, the effects of multi-body hydrodynamic interactions and the platform motion on power capture are also demonstrated. Since the power capture platform is symmetric about the wave incidence direction, only five WECs, WEC1-

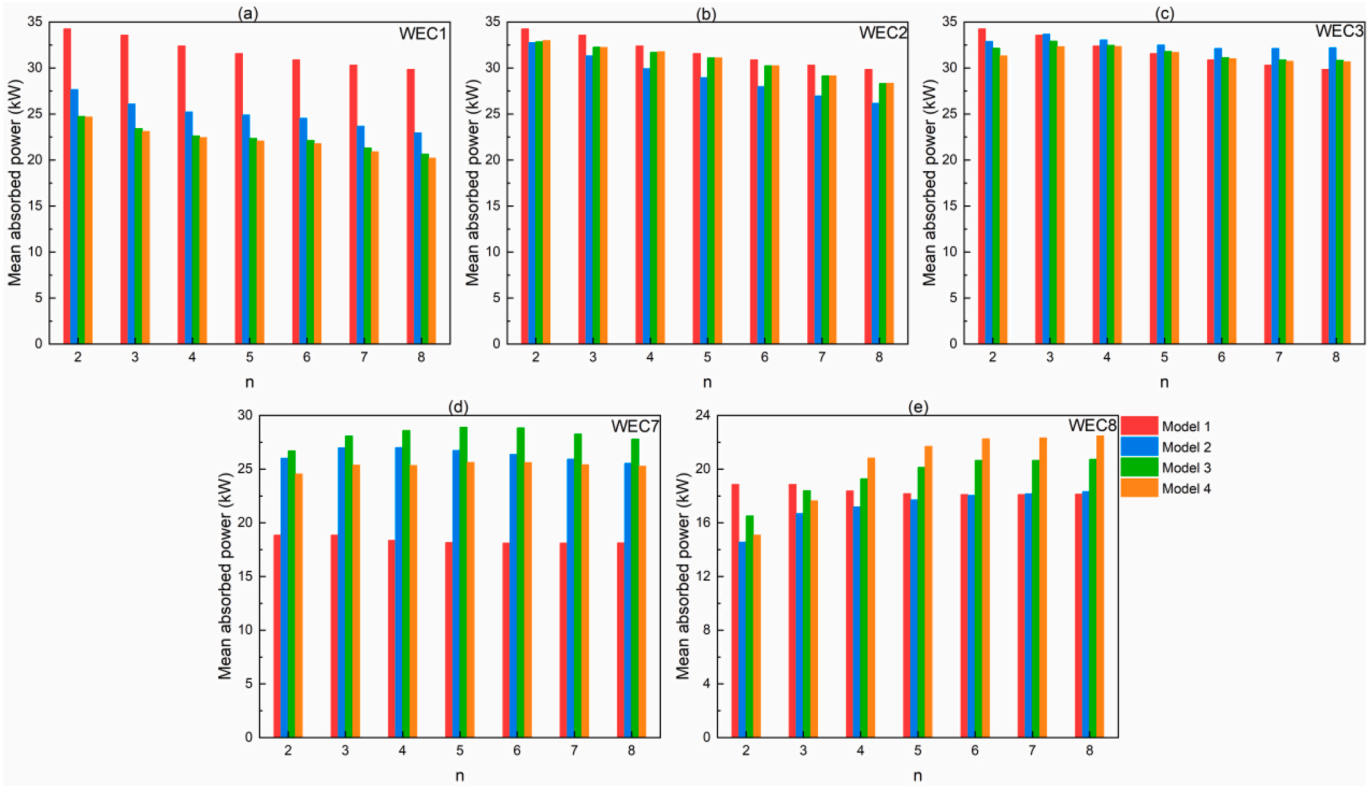

Fig. 14. Absorbed power of the WECs among different models for various *n* under LC1.

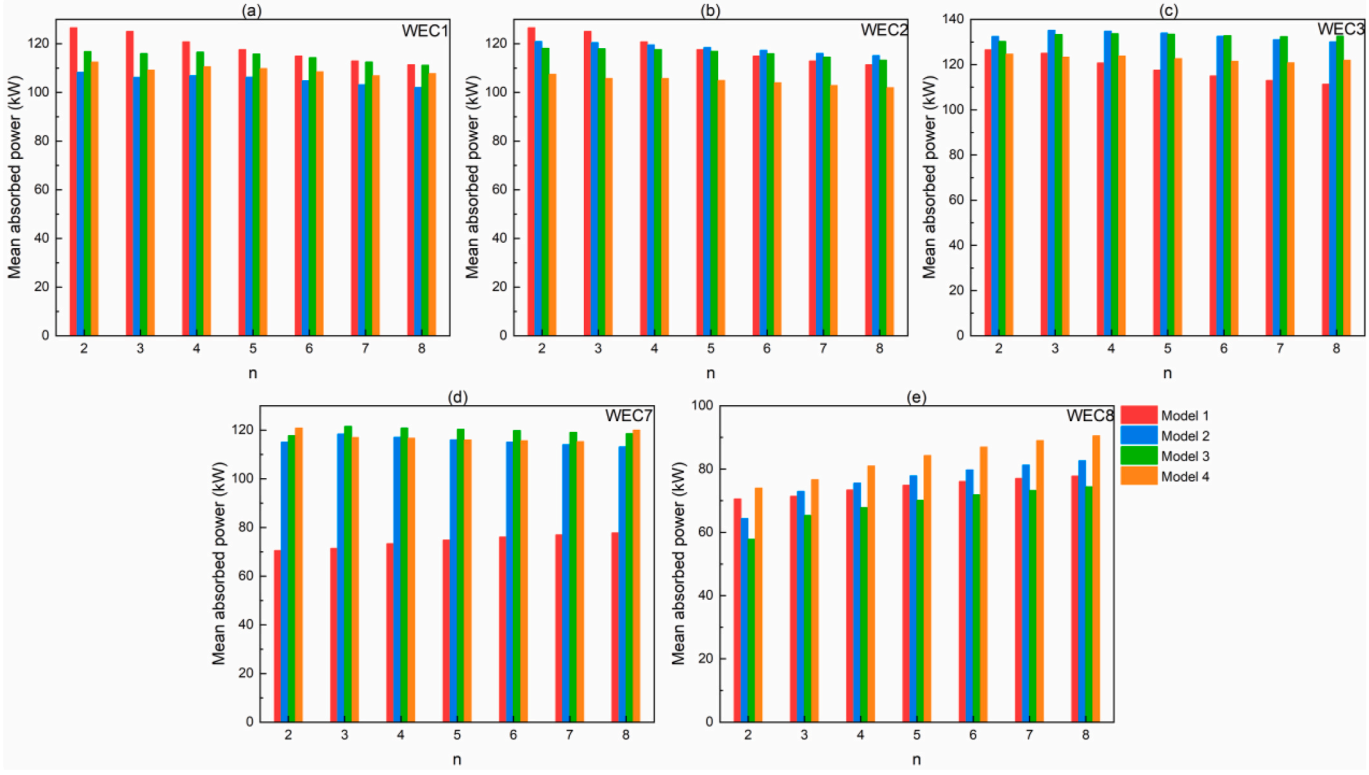

Fig. 15. Absorbed power of the WECs among different models for various *n* under LC2.

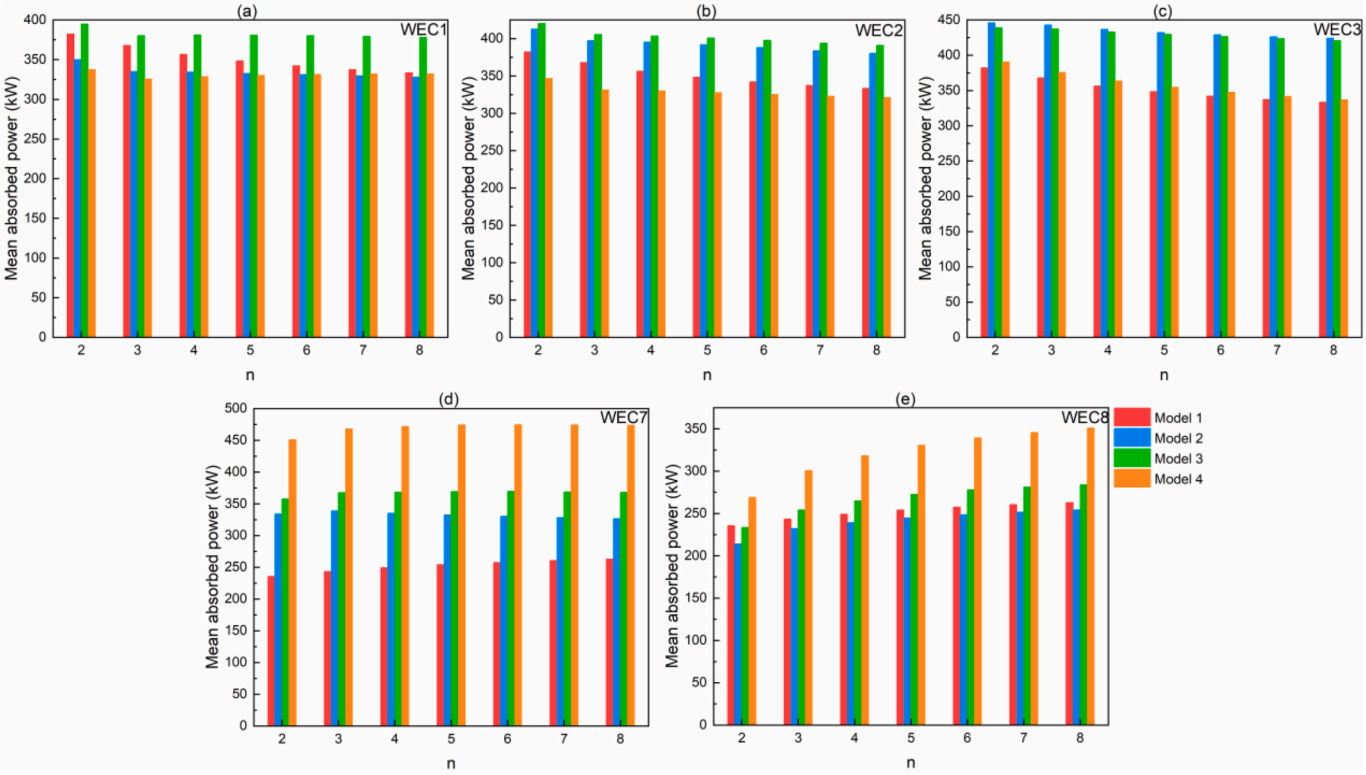

Fig. 16. Absorbed power of the WECs among different models for various n under LC3.

WEC3, WEC7, and WEC8, are considered in Section 5.5.1, while only two rows of WECs, Row1 and Row3, are investigated in Section 5.5.2. It is worth noting that, in order to evaluate the effects of the multi-body hydrodynamic interactions and platform motion on the wave energy conversion, another three models are set up as “Single”, “Wave farm”, “Power capture platform (fixed)". For the convenience of subsequent studies, these four models are defined as Model 1, Model 2, Model 3 and Model 4, respectively. Model 1 corresponds to a single WEC, Model 2 represents the WEC array, Model 3 is the fixed power capture platform, and Model 4 refers to the floating power capture platform.

5.5.1. *The individual WEC*

Figs. 14–16 demonstrate the mean absorbed power of the individual WECs among four models for various spreading components under three operational LCs. From Fig. 14(a)-14(b), it can be observed that the absorbed power of WEC1 and WEC2 decreases as the spreading exponent increases. This indicates that for these two WECs, the more focused the wave distribution, the better the power capture performance. From Fig. 14(c), it can be found that the variation pattern of the absorbed power of WEC3 regarding the spreading component is consistent among the latter three models, and WEC3 absorbs the most energy for $n = 3$. Among the models including WEC array, the performance of WEC3 is better as the spreading component is larger. From Fig. 14(d), it can be seen that among Models 1–4, WEC7 absorbs the most power for $n = 2$ or 3, $n = 4, n = 5$ and $n = 5$, respectively. Before this spreading component, the absorbed power has an increasing trend, while after it, the situation is opposite. This indicates that this spreading component is a threshold, which corresponds to a short-crested wave that is most conducive to the wave energy conversion of WEC7. In Fig. 14(e), it can be noticed that among the latter thre,e models, the absorbed power of WEC8 has an increasing trend regarding the spreading component. Meanwhile, for $n > 6$, the increase of the spreading component can no longer provide a significant enhancement to the performance of WEC8, which reflects that the wave distribution for $n = 6$ is already sufficient for WEC8 to achieve the optimal performance. For the performance of the identical WEC among different models, it can be observed from Fig. 14(a) that the absorbed power of WEC1 gradually decreases based on the Models 1–4 order. This phenomenon demonstrates that the multi-body hydrodynamic interactions as well as the platform motion are not conducive to the power capture of WEC1. From Fig. 14(b), it can be found that WEC2 has the best performance among Model 1 and the worst among Model 2. Meanwhile, the power captured by WEC2 among Model 3 is second only to that among Model 1. This indicates that the hydrodynamic interactions of the WEC array is not conducive to the performance of WEC2, but the platform interference with the wave field facilitates its wave energy conversion to some extent. Moreover, the platform motion slightly weakens its performance. As seen in Fig. 14(c), the captured power of WEC3 gradually decreases among the latter three models. In addition, the performance of WEC3 among Model 1 experiences from the best to the worst as the spreading exponent increases, which implies that the more focused the wave distribution is, the more significant the impact of multi-body hydrodynamic interactions on enhancing power absorption of WEC3. In Fig. 14(d), the power absorbed by WEC7 among the latter three models is much larger than that among Model 1. Meanwhile, WEC7 has the best and the worst performance among Model 3 and Model 4, respectively. This suggests that the platform interference with the wave field enhances the energy conversion of WEC7, while the platform motion impairs its performance. In addition, the difference in the power absorbed by WEC7 among Model 2 and Model 3 is more pronounced for large spreading components, while the situation among Model 2 and Model 4 is opposite. This means the platform interference with the wave field is more conducive to improve the performance of WEC7 for large spreading components, but the platform motion drastically impairs that advantage. In Fig. 14(e), the performance of WEC8 among Model 1 gradually transitions from being much better to being slightly weaker than that among Model 2 as the spreading component increases. This suggests that the hydrodynamic interactions of the WEC array can promote the energy conversion of WEC8 as the wave distribution becomes focused. For $n < 4$, the power absorbed by WEC8 among Model 3 is second only to that among Model

1, while that among Model 2 is the least. From this phenomenon, it can be inferred that as the wave distribution is relatively scattered, the platform interference with the wave field can improve the performance of WEC8 among Model 2 to a certain extent, but the platform motion undermines this advantage. In addition, for $n > 3$, the absorbed power of WEC8 progressively increases among the last three models. It can be reflected that when the spreading exceeds a certain threshold, the platform interference with the wave field as well as the platform motion improves the energy conversion of WEC8.

For the variation law of the absorbed power of the individual WEC regarding the spreading component under LC2 and LC3, and the difference of its power capture performance among four models, they will not be specifically developed here due to the space issue. The analysis of Figs. 15 and 16 can be referred to that of Fig. 14 above.

In order to assess the effects of multi-body hydrodynamic interactions as well as the platform motion on the performance of the individual WEC, an influence factor q_s is proposed, which can be expressed as:

$$q_s = \frac{P^i_{m,s}}{P^i_s} \tag{16}$$

where $P^i_{m,s}$ refers to the absorbed power of the i-th WEC among Model 2-Model 4; P^i_s represents the absorbed power of the i-th WEC among Model 1.

Figs. 17–19 illustrate the influence factor q_s of the individual WEC among three various models under three operational conditions with different spreading components. From Fig. 17(a), it can be observed that q_s of WEC1 are smaller than 1 among three models, indicating that the wave farm and the power capture platform are not conducive to its power absorption. Furthermore, q_s decreases progressively from Model 2 to Model 4, implying that both the platform interference with the wave field and the platform motion negatively affect the power capture performance of WEC1. The discrepancy of q_s between Model 2 and Model 3 is more pronounced than that between Model 3 and Model 4, suggesting that the platform interference with the wave field has a more significant impact on the power absorption of WEC1. As $n = 2$, the relative motion between the WEC1 and the platform can not significantly impair the power capture performance. Notably, the variation trend of q_s regarding the spreading component is consistent, with $n = 2$ and $n = 8$ representing the points of maximum and minimum values, respectively, and with $n = 3$ and $n = 6$ denoting the inflection points. This indicates that the negative effects of multi-body hydrodynamic interactions and platform motion on the performance of WEC1 are minimal and maximal as the wave distribution is the most scattered and the most focused, respectively. From Fig. 17(b), it can be seen that q_s of WEC2 are also smaller than 1 among three models. Additionally, q_s among Models 3 and 4 are larger than that among Model 2, while that among Models 3 and 4 is almost identical. This suggests that the platform interference with the wave field mitigates the negative impact of the hydrodynamic interactions within the WEC array on the power absorption of WEC2. Specifically, for $n = 5$, due to the platform interference with the wave field, the absorbed power of WEC2 among Models 3 and 4 is slightly less than that among Model 1. It is noteworthy that among Models 3 and 4, q_s initially increases and then decreases with the spreading component, while among Model 2, it shows a decreasing trend. This indicates that among Model 2, the negative impact of hydrodynamic interactions within the WEC array increases with the spreading component. Conversely, among Models 3 and 4, the adverse effects of multi-body hydrodynamic interactions on the power absorption initially weaken and then strengthen as the spreading component increases. In Fig. 17(c), it can be found that among Models 3–4, q_s of WEC3 is approximate to 1 as $n = 4$, while that is smaller and larger than 1 for $n < 4$ and $n > 4$, respectively. This indicates that the spreading component ($n = 4$) serves as a threshold for the power capture platform to benefit the energy conversion of WEC3. Additionally, among Model 2, WEC3 absorbs less energy than that among Model 1 as $n = 2$, while it performs better at any other spreading component. Moreover, q_s of WEC3 among Model 2 is larger than that among Models 3–4, suggesting that the presence of the platform is detrimental to the energy conversion of WEC3 in the WEC

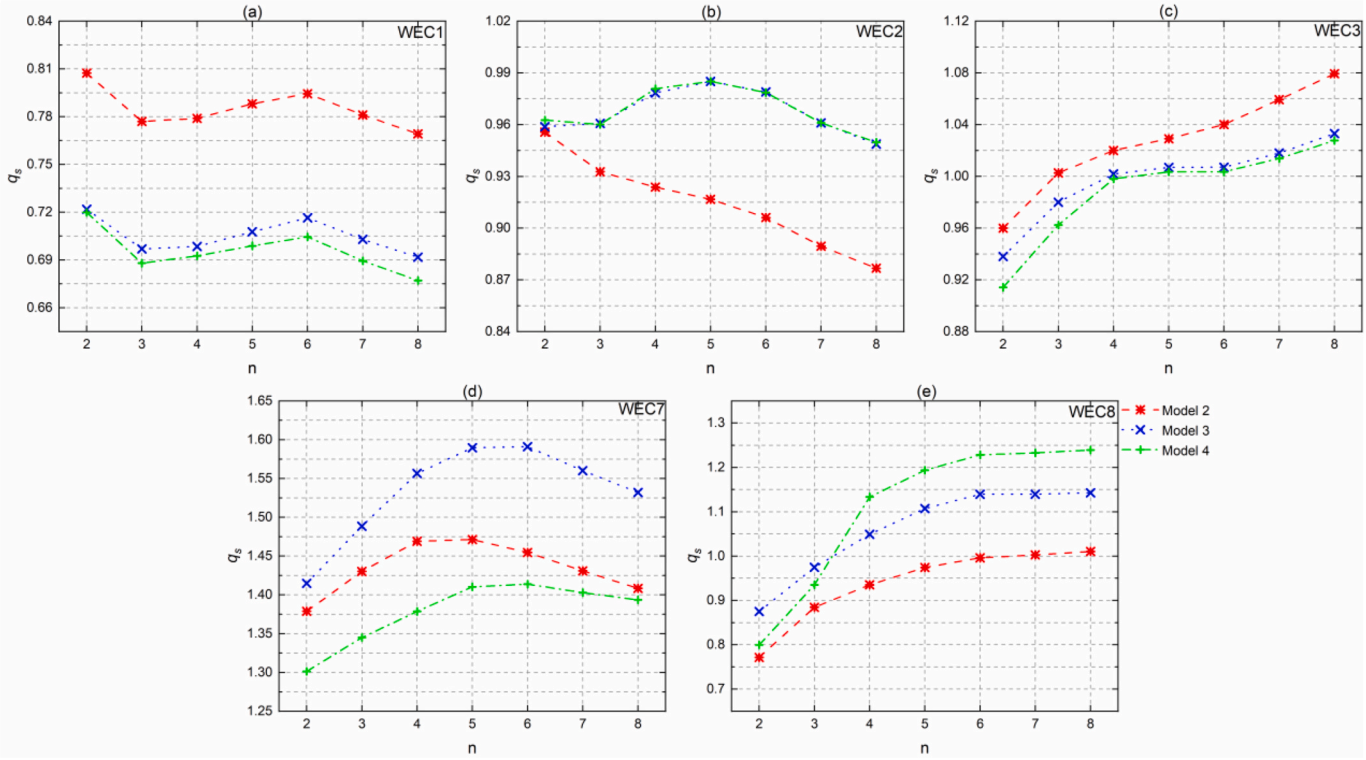

Fig. 17. q_s of the WECs among different models for various n under LC1.

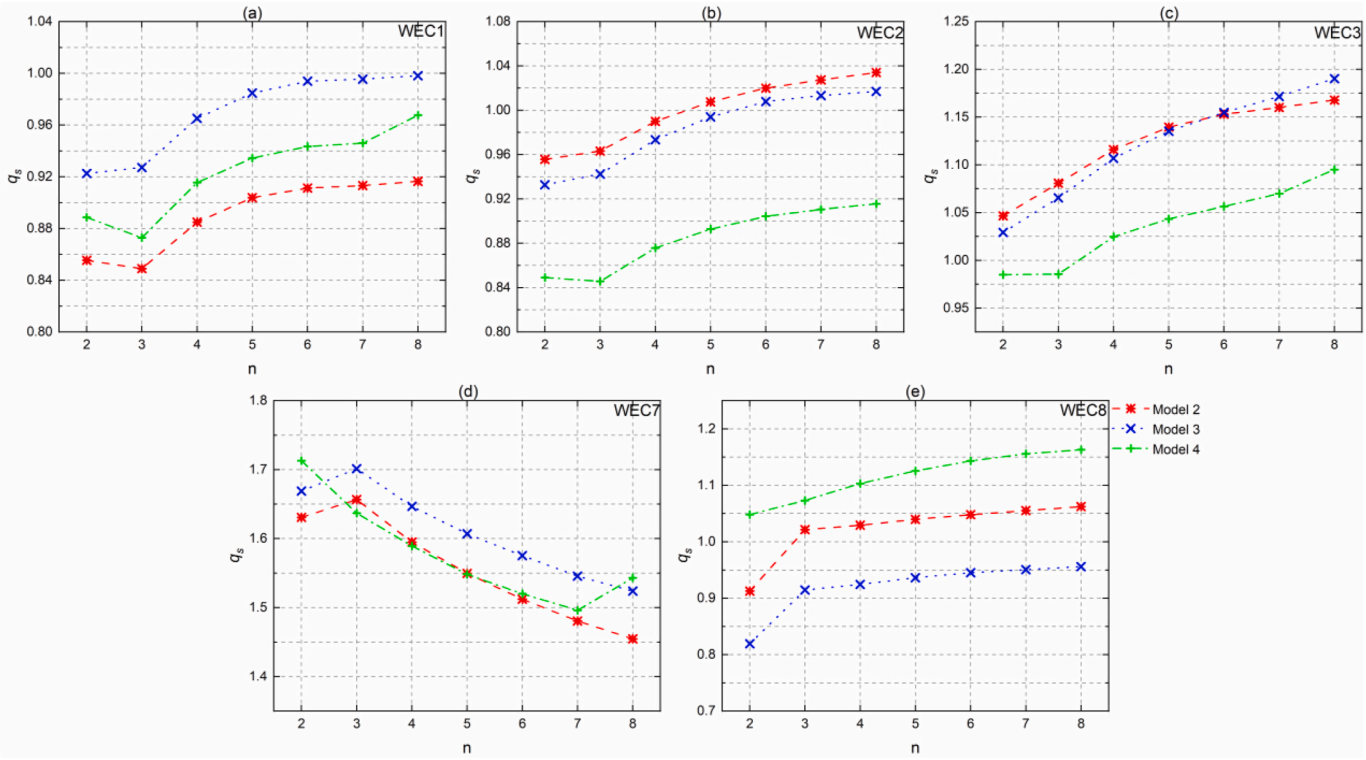

Fig. 18. q_s of the WECs among different models for various n under LC2.

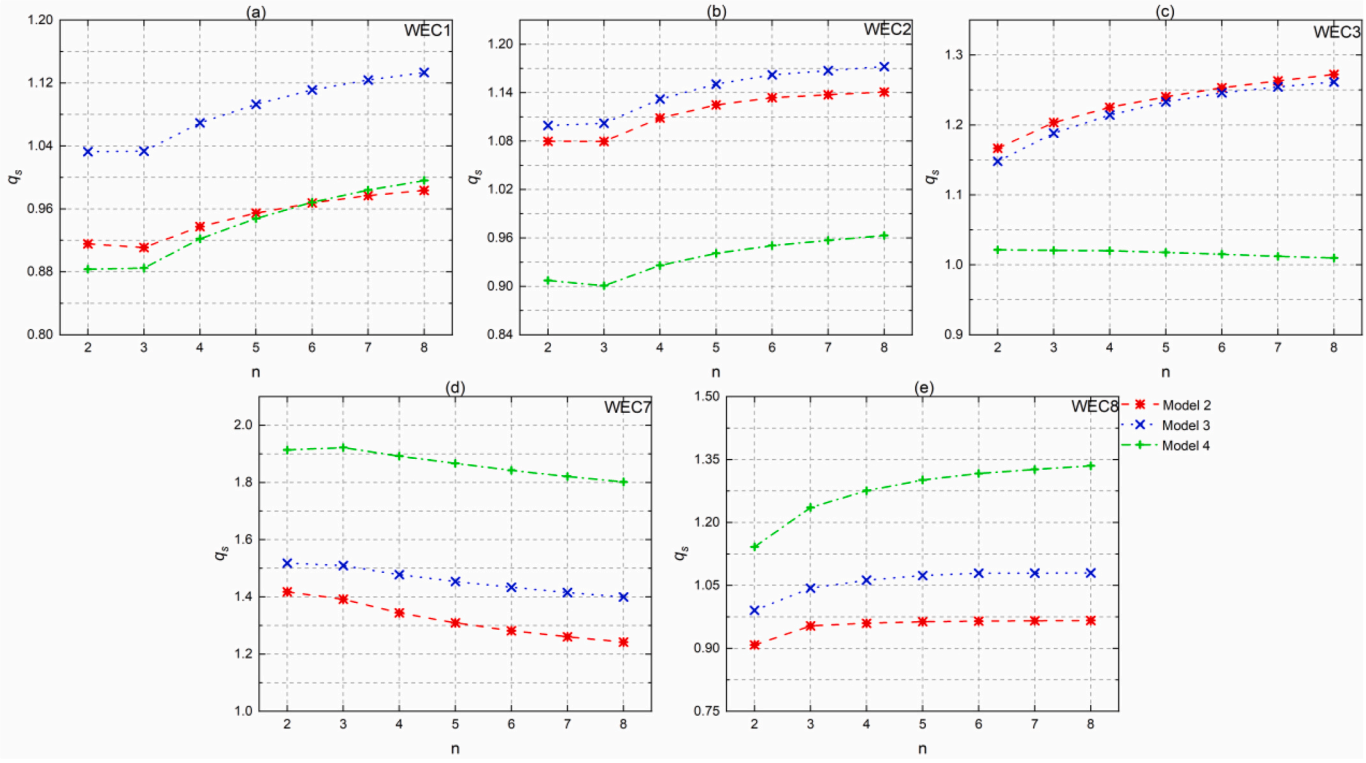

Fig. 19. q_s of the WECs among different models for various n under LC3.

array. For $n < 4$, q_s of WEC3 among Model 3 is larger than that among Model 4, while for $n > 3$, that is similar among both models. This implies that when the wave distribution is relatively scattered, the platform motion further hinders the performance of WEC3, with the basis of the platform interference with the wave field. Additionally, q_s of WEC3 shows an increasing trend with the spreading, transitioning from smaller than 1 to larger than 1, suggesting that the performance of WEC3 improves under short-crested waves with more focused energy. As shown

in Fig. 17(d), q_s of WEC7 is larger than 1 among three models, indicating that both the wave farm and the power capture platform concepts enhance its energy absorption. q_s among Model 2 is larger than that among Model 4 but smaller than that among Model 3, which suggests that the platform interference with the wave field significantly enhances the performance of WEC7, while the platform motion diminishes this advantage. Additionally, the variation trend in q_s regarding the spreading component is similar among three models, initially rising and then falling. This indicates that the maximum advantage of the wave farm and the power capture platform concepts is realized for a specific spreading component. In Fig. 17(e), q_s of WEC8 among Model 2 is smaller than 1 for $n < 6$, and approximate to 1 for $n > 5$. This demonstrates that only when the wave distribution is relatively focused does the wave farm concept not hinder the power capture performance of

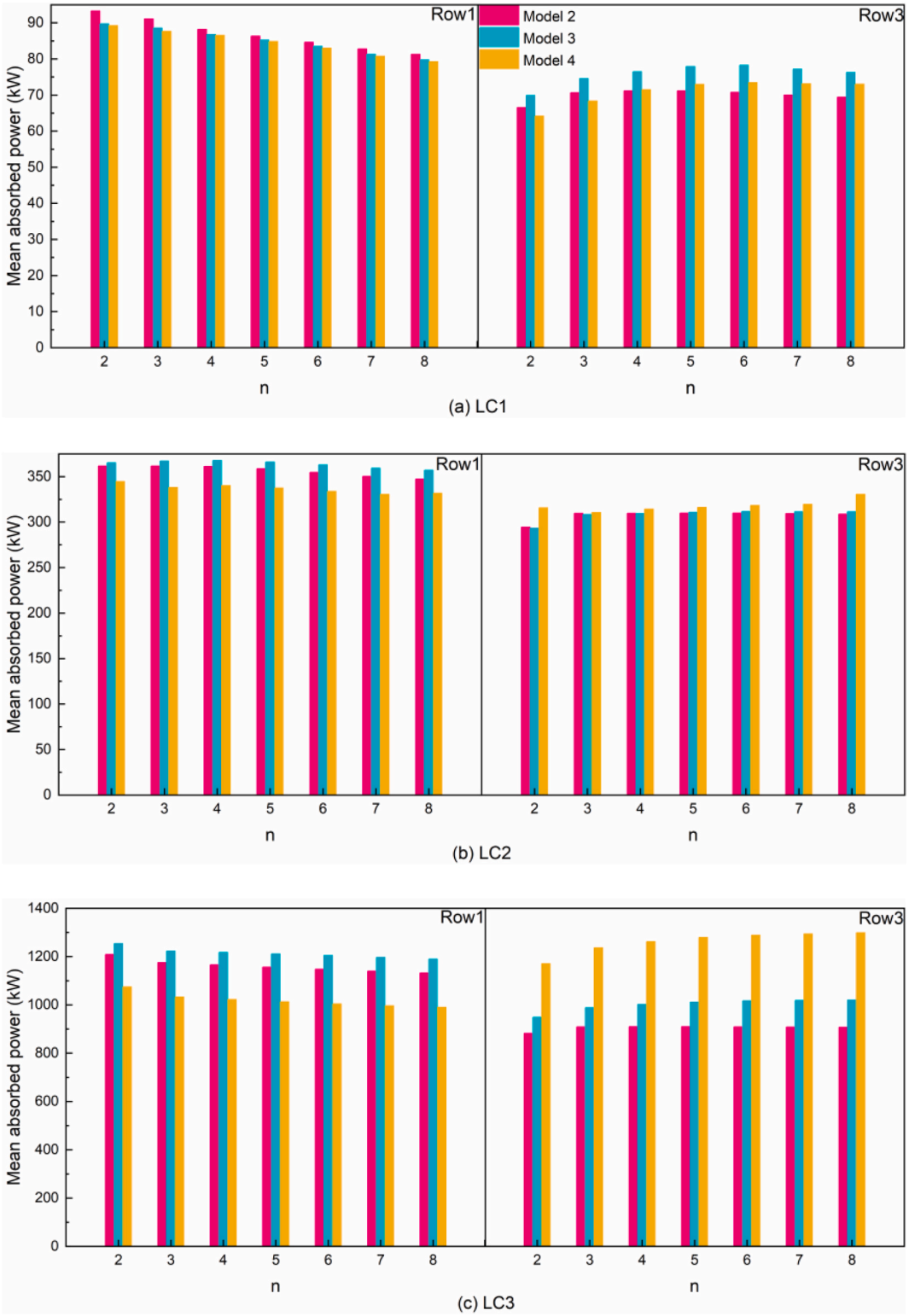

Fig. 20. Absorbed power of the WEC rows among different models for various n under three operational LCs.

WEC8. For $n < 4$, q_s of WEC8 among Models 3–4 is smaller than 1, indicating that the power capture platform concept is detrimental to the power absorption when the wave distribution is relatively scattered. Furthermore, for $n < 4$, q_s of WEC8 among Model 3 is the largest, while among Model 2, it is the smallest. Meanwhile, for $n > 3$, q_s among Model 4 reaches the maximum value, while among Model 2, it remains the smallest. This means that Model 2 is the least conducive multi-body design for the power absorption of WEC8 when the wave distribution is relatively scattered, while Model 4 is the best concept when the wave distribution is relatively focused. Notably, q_s of WEC8 shows an increasing trend with the spreading component, similar to WEC3.

Since the wave parameters of LC2 and LC3 are different from those of LC1, it remains unknown whether the multi-body design concept enhances the power absorption of the individual WEC. However, due to the space issue, it will not be specifically developed here. The analysis of Figs. 18 and 19 can be referred to the analysis of Fig. 17 above. What can be confirmed is that the wave distribution, the multi-body hydrodynamic interactions, and the platform motion still serves as the basis of the analysis.

5.5.2. The WEC row

Fig. 20 illustrates the mean absorbed power of WEC arrays under various spreading components among three models under three operational conditions. From Fig. 20(a), it can be observed that under LC1, the absorbed power of Row1 is larger than that of Row3. This is due to the more favorable positions of the WECs among Row1, which facilitate the excitation of larger vertical motion. The absorbed power of Row1 decreases with the spreading component, indicating that the more focused the wave distribution is, the poorer the power capture performance of Row1. Furthermore, the power absorption of Row1 is the highest among Model 2 and the lowest among Model 4, suggesting that the platform-induced wave field interference and platform motion are detrimental to the power absorption of Row1. For Row3, its performance is best among Model 3, implying that platform-induced wave field interference can enhance the power absorption of Row3. The variation trend of power absorption for Row3 regarding the spreading component shows an initial increase followed by a decrease among Models 2–3. In contrast, among Model 4, the power capture performance of array3 steadily improves for $n < 7$. When the wave distribution is relatively focused, the power absorption of Row3 among Model 4 remains almost unchanged. These phenomena suggest that for Models 2–3, the multi-body hydrodynamic interactions can maximize advantages at a specific spreading component. Meanwhile, for Model 4, considering both platform motion and multi-body hydrodynamic interactions, the power capture performance of Row3 does not significantly change with the increase in spreading component. Moreover, the power absorbed by Row3 among Model 2 is more than that among Model 4 when the spreading component is relatively small, and vice versa when the spreading component is relatively large. This implies that whether the platform's presence is beneficial for the power absorption of Row3 depends on the wave distribution. As shown in Fig. 20(b), under LC2, the absorbed power of Row1 is also more than that of Row3. Row1 absorbs the most energy among Model 3 and the least among Model 4, indicating that the platform-induced wave field interference can promote power absorption, but the platform motion significantly reduces this advantage. For $n < 6$, the power capture performance of Row1 among Models 2–3 shows little difference, whereas for $n > 4$, it presents a downward trend with the spreading component. Among Model 4, the power absorption of Row1 generally decreases with the spreading component. Additionally, Row3 absorbs the most energy among Model 4, while its performance is roughly the same among the other two models, indicating that the platform motion can enhance the power absorption of Row3, whereas the platform-induced hydrodynamic interference do not significantly improve the power capture performance of Row3 among the WEC array. When the wave distribution is the most scattered, Row3 absorbs the least power among Models 2–3, while its power absorption changes little with the spreading component for $n > 2$. Meanwhile, the absorbed power of Row3 among Model 4 generally shows an overall upward trend with the spreading component, but its power absorption for $n = 2$ is more than that for $n = 3$. These phenomena suggest that Row3 performs best under short-crested waves with more focused distribution. In Fig. 20(c), it can be found that under LC3, the absorbed power of Row1 decreases with the spreading component. Additionally, the power capture performance of Row1 is the best among Model 3 and worst among Model 4. For Row3, its power absorption increases with the spreading component, indicating that Row3 performs better under short-crested waves with more focused energy. This phenomenon is because the positions of the WECs among Row3 are aligned with the incident wave direction. However, among Model 2, there is no significant difference in power absorption of Row3 for $n > 2$. Moreover, Row3 absorbs the least power among Model 2 and the most among Model 4, demonstrating that on the basis of platform-induced wave field interference, the platform motion can further enhance the power absorption of Row3. Notably, the power absorbed by Row3 among Model 4 significantly exceeds that among Models 2 and 3, implying that the floating power capture platform concept contributes significantly to the power absorption of Row3. Interestingly, the power absorbed by Row3 among Model 4 is not less than that of Row1 as expected. Instead, the performance of Row3 among Model 4 is significantly better than that of Row1, which can be inferred that the contribution of the platform motion to the power absorption of Row3 far outweighs the disadvantage of its layout.

To evaluate the impact of multi-body hydrodynamic interference and platform motion on the energy capture performance of WEC arrays, an influence factor is proposed, which can be expressed as follows:

$$q_r = \frac{\sum_{i=j+1}^{j+3} P_{m,s}^i}{\sum_{i=j+1}^{j+3} P_s^i}, j = 0 \text{ or } 6 \tag{17}$$

Fig. 21 illustrates the influence factor q_r of the WEC arrays for different spreading components among three models under three operational conditions. From Fig. 21(a), it can be observed that under LC1, q_r of Row1 is smaller than 1, indicating that the wave farm and power capture platform concepts are detrimental to its power absorption. Additionally, q_r of Row1 is the highest among Model 2 and the lowest among Model 4, suggesting that the presence of the platform further diminishes the power capture performance of Row1. Among Model 2, q_r of Row1 reaches minimal for $n = 3$ and maximal for $n = 6$. In fact, the performance of Row1 among Model 2 does not vary significantly with different spreading components, showing that the wave farm concept does not noticeably change the performance of Row1 with various wave distributions. Meanwhile, among Models 3–4, q_r of Row1 initially increases and then decreases with the spreading component, demonstrating that the power absorption of Row1 is more significantly affected by the wave directionality among these two models compared to Model 2. Additionally, q_r of Row is larger than 1, which means that the wave farm and power capture platform concepts promote its energy conversion. Moreover, q_r of Row3 is the highest among Model 3, reflecting that the platform-induced wave field interference enhance its performance, while the platform motion reduces this advantage. It is noteworthy that the spreading component ($n = 4$) marks the point where the performance of Row3 among Model 2 begins to fall behind that among Model 4. This implies that for $n \geq 4$, the fixed power capture platform concept outperforms the wave farm concept. Furthermore, q_r of Row3 shows an initial increase followed by a decrease with the spreading component, though the decreasing trend is relatively gentle compared to the increasing trend. This phenomenon indicates that when the spreading component is relatively small, the power absorption of Row3 is more influenced by the multi-body hydrodynamic interactions and platform motion. As seen in Fig. 21(b), under LC2, q_r of Row1 among Model 4 is

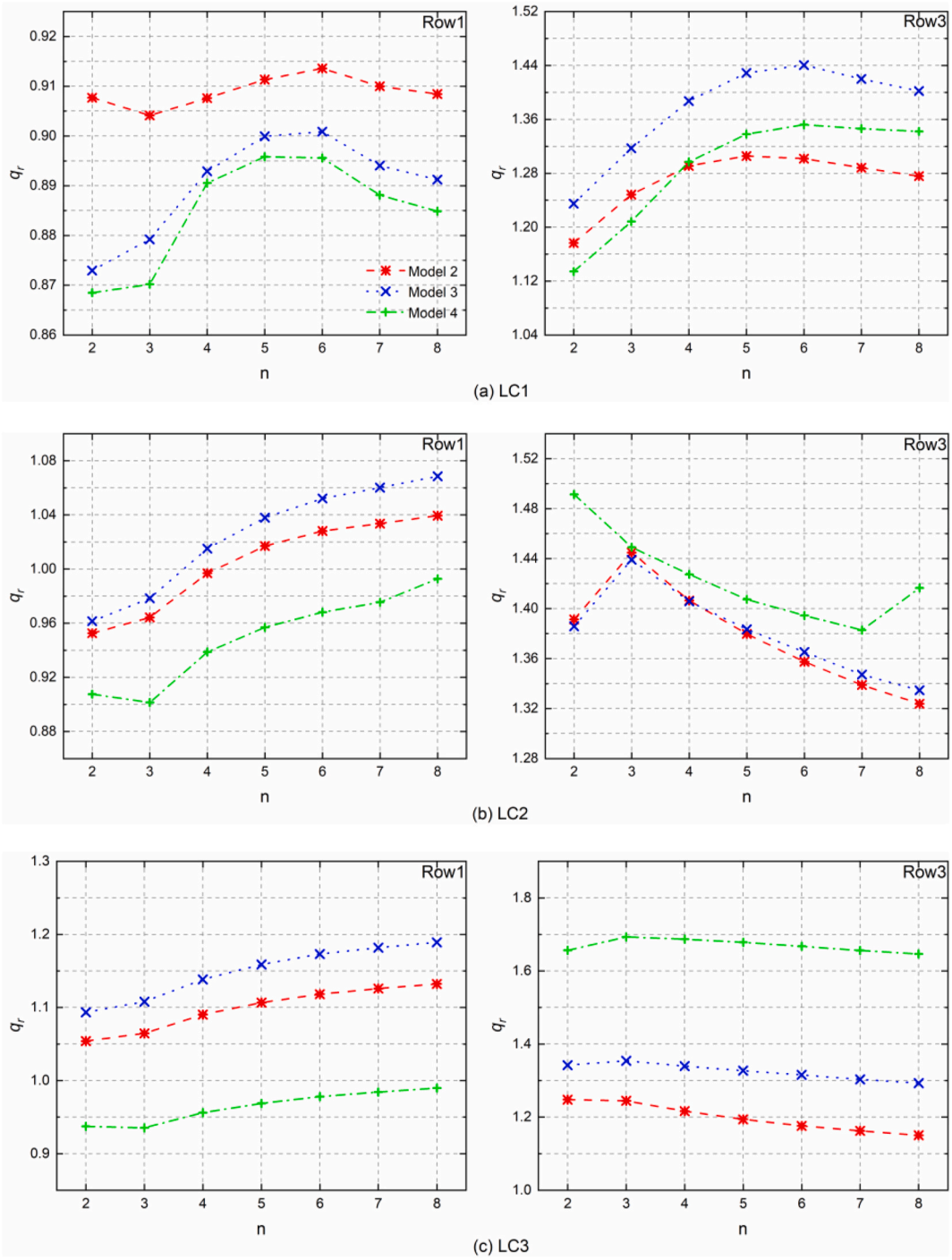

Fig. 21. q_r of the WEC rows among different models for various n under three operational LCs.

smaller than 1, indicating that the floating energy capture platform concept is detrimental to its power absorption. Simultaneously, q_r of Row1 among Models 2 and 3 is larger than 1 for $n > 4$ and $n > 3$, respectively. This implies that when the wave distribution is more focused, the power capture performance of Row1 among Models 2–3 is enhanced due to the multi-body hydrodynamic interactions. Additionally, q_r of Row1 is larger among Model 3 than that among Model 2, suggesting that compared to the wave farm concept, the fixed power capture platform concept is more beneficial for the power absorption of Row1. Furthermore, q_r of Row1 among Models 2–3 shows an upward trend with the spreading component. Although q_r of Row1 among Model 4 is minimal for $n = 3$, the overall trend is also upward, showing that the more focused the wave directionality is, the more beneficial the multi-body hydrodynamic interactions and platform motion are to the power absorption of Row1. For Row3, q_r is larger than 1, demonstrating that the wave farm and power capture platform concepts are beneficial for enhancing its performance. q_r of Row3 among Model 4 is larger than that among the other two models, which means that the floating power capture platform concept is more advantageous for enhancing the performance of Row3. Meanwhile, q_r of Row3 among Model 3 is slightly larger than that among Model 2 for relatively large spreading components, while it is similar for relatively small spreading components, implying that the platform-induced hydrodynamic interference does not significantly improve the power absorption of Row3 among the WEC

array. Notably, for $n = 3$, the performance of Row3 is almost identical among the three models, demonstrating that for this spreading component, the presence of the platform does not provide a significant advantage. Moreover, based on the variation trend of q_r regarding the spreading component, it can be inferred that the multi-body design concept contributes more to the power absorption of Row3 when the wave distribution is more scattered. FromFig. 21(c), it can be found that under LC3, q_r of Row1 among Models 2–3 is larger than 1, while among Model 4 it is smaller than 1. Meanwhile, q_r of Row1 among Model 3 is larger than that among Model 2. These phenomena indicate that both the hydrodynamic interactions within the WEC array and the platform-induced wave field interference can promote the power absorption of Row1, while the platform motion has the opposite impact. More specifically, the floating power capture platform concept is detrimental to the power absorption of Row1. Overall, q_r of Row1 shows an upward trend with the spreading component. This implies that for the power absorption of Row1, the more focused the wave distribution is, the more beneficial the designs of Models 2–3 are, while the design of Model 4 is less advantageous. Additionally, q_r of Row3 is larger than 1, demonstrating that the wave farm and power capture platform concepts can enhance its power absorption. q_r of Row3 among Model 4 is the highest, and the lowest among Model 2, while the difference is significant. This suggests that the floating platform can greatly enhance the performance of Row3. Moreover, q_r of Row3 shows a downward trend with the spreading component. This phenomenon reflects that for the power absorption of Row3, the advantage brought by the multi-body design concept is more obvious under more focused short-crested waves.

5.5.3. The WEC array

Fig. 22 illustrates the total absorbed energy of the WEC array among three models for different spreading components under three operational conditions. From Fig. 22(a), it can be observed that under LC1, the power absorption of the WEC array shows slight variation for lower spreading components, but declines as the spreading component increases. This suggests that the performance of WEC array in capturing power decreases when the wave directionality is more focused. Additionally, the power absorbed by the WEC array is more among Model 2 compared to Model 3, indicating that the platform interference with the wave field is detrimental to power absorption of the WEC array. However, the situation is opposite for $n > 3$ under LC2, reflecting that the platform interference with the wave field enhances the power absorption of the WEC array under focused short-crested wave. Furthermore, the least energy is absorbed among Model 4 compared to the other two models, which demonstrates that a floating platform significantly weakens the power capture performance of the WEC array. In Fig. 22(b), it is evident under LC2 that the WEC array absorbs the most energy among Model 3 and the least among Model 4. This indicates that the platform interference with the wave field is disadvantageous to power absorption of the WEC array. Overall, the power absorbed by the WEC arrays among Models 2–3 shows an initially increasing and then decreasing trend regarding the spreading component, while the power capture performance among Model 4 shows no clear trend regarding the spreading component. However, there is no significant difference in energy absorption of the WEC array for different spreading components, which reflects that the wave directionality does not significantly affect the power capture performance of the WEC array. As seen in Fig. 22(c), under LC3 that the power absorbed by the WEC array is the highest among Model 3 and the lowest among Model 2. This implies that the concept of power capture platform enhances the performance of the WEC array, although the floating platform diminishes this advantage to some extent. Additionally, among Model 2, there is a slight downward trend in power absorption of the WEC array with the spreading

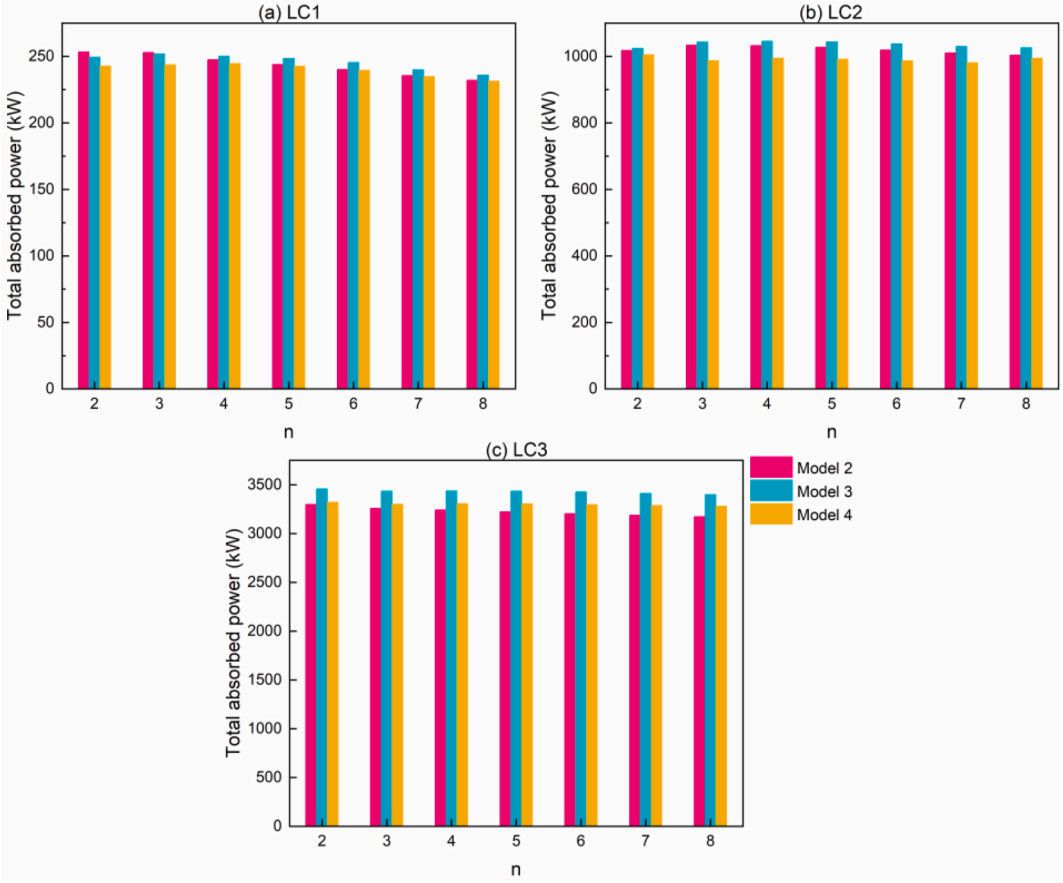

Fig. 22. Absorbed power of the WEC array among different models for various n under three operational LCs.

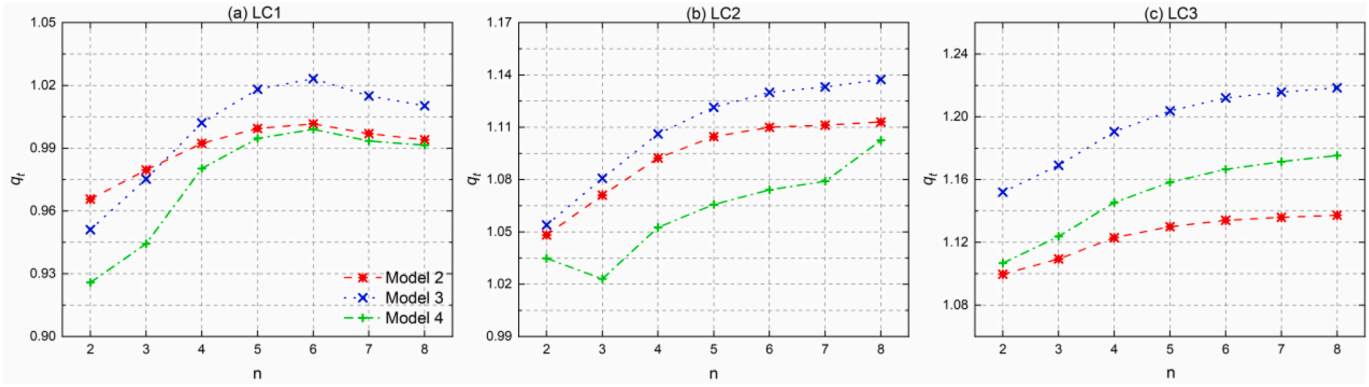

Fig. 23. q_t of the WEC array among different models for various n under three operational LCs.

component, whereas its performance among Models 3–4 shows slight variation for different spreading components. This indicates that the power absorption of the WEC array is less affected by the wave distribution.

To assess the impact of the multi-body hydrodynamic interactions and platform motion on the power capture performance of the WEC array, an influence factor is proposed, expressed as:

$$q_t = \frac{\sum_{i=1}^{9} P_{m,s}^{i}}{\sum_{i=1}^{9} P_{s}^{i}} \tag{18}$$

Fig. 23 illustrates q_t of the WEC array among three models for different spreading components under three operational conditions. From Fig. 23(a), it can be observed that under LC1, q_t of the WEC array among Models 2–4 are smaller than 1, indicating that the wave farm and floating power capture platform concepts are not favorable for its power absorption. Meanwhile, q_t of the WEC array among Model 3 are smaller than 1 for $n < 5$ but larger than 1 for other spreading components, implying that Model 3 is beneficial for the power absorption under more focused short-crested waves. Additionally, q_t of the WEC array is minimal among Model 4, suggesting that the floating platform weakens the performance of the WEC array among Model 2. Meanwhile, for $n < 4$, q_t of the WEC array among Model 2 is larger than that among Model 3, but the reverse is true for other spreading components, which reflects that the addition of a fixed platform weakens the advantage of wave farm when the wave distribution is relatively scattered. It is notable that for $n > 5$, the difference in q_t of the WEC array between Model 2 and Model 4 is slight, showing that a floating platform may not significantly affect the power absorption of the WEC array among Model 2 under the focused wave distribution. Furthermore, q_t of the WEC array shows an initial increasing and then decreasing trend concerning the spreading component, with a stronger increasing trend observed. This demonstrates that the performance of the WEC array is more influenced by the wave directionality when the spreading component is relatively small. As shown in Fig. 23(b), under LC2, q_t of the WEC array is larger than 1, indicating that all three models are favorable for its power absorption. q_t of the WEC array is the largest among Model 3 and the smallest among Model 4, which implies that the platform-induced wave field interference enhances the power capture performance of the WEC array among Model 2, whereas the platform motion has the opposite impact. Additionally, q_t of the WEC array among Models 2–3 shows an increasing trend with the spreading component, demonstrating that the designs of Models 2–3 contribute more to the energy absorption of the WEC array under more focused wave distribution. Meanwhile, apart from the spreading component ($n = 2$), q_t of the WEC array among Model 4 also increase with the spreading component. In Fig. 23(c), it can be seen that under LC3, q_t of the WEC array is also larger than 1. Furthermore, q_t of the WEC array is maximal among Model 3 and minimal among Model 2, indicating that the fixed platform enhances its power capture performance more than the floating platform. The variation law of q_t of the WEC array concerning the spreading component shows an upward trend among all three models, which reflects that the power absorption of the WEC array benefits more from the concepts of wave farm and power capture platforms when the wave distribution is more focused.

6. Conclusion

This paper investigates the dynamic behavior of a novel power capture platform under short-crested wave conditions, which is composed of a semi-submersible platform and multiple point-absorbed WECs. Three-dimensional potential theory and BEM are used to validate the numerical model and resolve the wave excitation forces. After the mathematical model of the short-peak wave is derived, time-domain simulations are conducted to analyze the effects of the wave directionality on the platform motion, mooring line tension, and the power capture performance of the WEC array. Five LCs are selected, including three operational conditions and two extreme conditions. Based on the results, some important conclusions are summarized as follows.

(1) Under LC1, the mean surge response shows slight variation across different spreading components, whereas under LC2-LC5, there is an increasing trend regarding the spreading component. A transition occurs in the mean heave and pitch responses under LC1 when the spreading component exceeds 3, while under LC2, they are relatively small for the spreading components of 2 and 8. Meanwhile, under LC3-LC5, the mean heave and pitch responses remain almost constant across the spreading components.
(2) Under LC1-LC4, the STD of the surge response shows an increasing trend regarding the spreading component, whereas under LC5, it exhibits a decreasing trend. Under LC1 and LC4, the STD of the heave response increases with the spreading component, while under LCs2-3 and LC5, it remains almost constant. Overall, the STD of the pitch response shows an increasing trend regarding the spreading component under LC1-LC5.
(3) For the #5 tension response, the variation of spreading component has a slight impact on its mean value and STD under LC1-LC3. However, under LC4-LC5, both the mean value and STD of the #5 tension response exhibit a decreasing trend regarding the spreading component. Regarding the maximum value of the #5 tension response, the spreading component has slight effects under LC1-LC3. In contrast, under LC4 and LC5, there is a significant difference in the maximum responses of the #5 tension across different spreading components.
(4) Under LC1, WEC1 absorbs significantly more energy among Model 1 compared to the other three models, whereas the opposite trend is observed for WEC7. Under LC2, the energy conversion of WEC7 is notably better among the multi-body

models than that among Model 1. Under LC3, the power absorption of WECs 7–8 among Model 4 is markedly superior to that among the other three models.

(5) Under LC1 and LC3, Row1 exhibits a decreasing trend in power absorption among any model regarding the spreading component. Meanwhile, under LC1, Row1 absorbs the most energy among Model 2, whereas under LC2-LC3, it demonstrates the optimal performance among Model 3. For Row3, under LC1, Model 3 is the best design for its power capture. Furthermore, under LC2-LC3, Row3 absorbs more energy among Model 4 compared to the other two models.

(6) For the WEC array, under LC1, there is a slight decreasing trend in power absorption regarding the spreading component. Under LC2-LC3, the power absorption of the WEC array among any model shows slight variation across different spreading components. Furthermore, under LC1-LC3, Model 3 can be identified as the best multi-body design for the WEC array.

The above findings can provide some insights into the design of power capture platforms. In future work, the efforts will focus on optimizing the platform system, WEC floaters, and the layout of the WEC array to enhance the platform stability and power capture performance of the WEC array.

CRediT authorship contribution statement

Haitao Wu: Writing – original draft, Visualization, Validation, Methodology, Formal analysis, Data curation, Conceptualization. **Zhiming Yuan:** Writing – review & editing, Supervision.

Data availability

Data will be made available on request.

Declaration of competing interest

The authors declare that they have no known competing financial interests or personal relationships that could have appeared to influence the work reported in this paper.

Acknowledgement

The first author would like to thank Siqi Wu for the patience and support on his research.

Appendix A

For the power capture platform as shown in Fig. 3, there are ten bodies and nine hinged constraints. Therefore, the constraint matrix $\boldsymbol{H}$ is given as follows:

$$\boldsymbol{H}=\begin{bmatrix} \boldsymbol{H_{P,W1}} & \boldsymbol{H_{W1}} & \mathbf{0} & \mathbf{0} & \mathbf{0} & \mathbf{0} & \mathbf{0} & \mathbf{0} & \mathbf{0} & \mathbf{0} \\ \boldsymbol{H_{P,W2}} & \mathbf{0} & \boldsymbol{H_{W2}} & \mathbf{0} & \mathbf{0} & \mathbf{0} & \mathbf{0} & \mathbf{0} & \mathbf{0} & \mathbf{0} \\ \boldsymbol{H_{P,W3}} & \mathbf{0} & \mathbf{0} & \boldsymbol{H_{W3}} & \mathbf{0} & \mathbf{0} & \mathbf{0} & \mathbf{0} & \mathbf{0} & \mathbf{0} \\ \boldsymbol{H_{P,W4}} & \mathbf{0} & \mathbf{0} & \mathbf{0} & \boldsymbol{H_{W4}} & \mathbf{0} & \mathbf{0} & \mathbf{0} & \mathbf{0} & \mathbf{0} \\ \boldsymbol{H_{P,W5}} & \mathbf{0} & \mathbf{0} & \mathbf{0} & \mathbf{0} & \boldsymbol{H_{W5}} & \mathbf{0} & \mathbf{0} & \mathbf{0} & \mathbf{0} \\ \boldsymbol{H_{P,W6}} & \mathbf{0} & \mathbf{0} & \mathbf{0} & \mathbf{0} & \mathbf{0} & \boldsymbol{H_{W5}} & \mathbf{0} & \mathbf{0} & \mathbf{0} \\ \boldsymbol{H_{P,W7}} & \mathbf{0} & \mathbf{0} & \mathbf{0} & \mathbf{0} & \mathbf{0} & \mathbf{0} & \boldsymbol{H_{W6}} & \mathbf{0} & \mathbf{0} \\ \boldsymbol{H_{P,W8}} & \mathbf{0} & \mathbf{0} & \mathbf{0} & \mathbf{0} & \mathbf{0} & \mathbf{0} & \mathbf{0} & \boldsymbol{H_{W7}} & \mathbf{0} \\ \boldsymbol{H_{P,W9}} & \mathbf{0} & \mathbf{0} & \mathbf{0} & \mathbf{0} & \mathbf{0} & \mathbf{0} & \mathbf{0} & \mathbf{0} & \boldsymbol{H_{W8}} \end{bmatrix}_{(4\times6+5\times3)\times(6\times10)} \tag{A1}$$

where,

$$\boldsymbol{H_{P,Wi}}=\begin{bmatrix} 1 & 0 & 0 & 0 & z_{P,Wi} & -y_{P,Wi} \\ 0 & 1 & 0 & -z_{P,Wi} & 0 & x_{P,Wi} \\ 0 & 0 & 1 & y_{P,Wi} & -x_{P,Wi}0 & 0 \\ 0 & 0 & 0 & 0 & & 1 \end{bmatrix},(i=1\sim6) \tag{A2}$$

$$\boldsymbol{H_{P,Wj}}=\begin{bmatrix} 1 & 0 & 0 & 0 & z_{P,Wj} & -y_{P,Wj} \\ 0 & 1 & 0 & -z_{P,Wj} & 0 & x_{P,Wj} \\ 0 & 0 & 1 & y_{P,Wj} & -x_{P,Wj} & 0 \\ 0 & 0 & 0 & 1 & 0 & 0 \\ 0 & 0 & 0 & 0 & 0 & 1 \end{bmatrix},(j=7-9) \tag{A3}$$

$$\boldsymbol{H_{Wi}}=\begin{bmatrix} -1 & 0 & 0 & 0 & -z_{Wi} & y_{Wi} \\ 0 & -1 & 0 & z_{Wi} & 0 & -x_{Wi} \\ 0 & 0 & -10 & -y_{Wi} & x_{Wi} & 0-1 \\ 0 & 0 & & 0 & 0 & \end{bmatrix},(i=1\sim6) \tag{A4}$$

$$\boldsymbol{H_{Wj}} = \begin{bmatrix} -1 & 0 & 0 & 0 & -z_{Wj} & y_{Wj} \\ 0 & -1 & 0 & z_{Wj} & 0 & -x_{Wj} \\ 0 & 0 & -1 & -y_{Wj} & x_{Wj} & 0 \\ 0 & 0 & 0 & -1 & 0 & 0 \\ 0 & 0 & 0 & 0 & 0 & -1 \end{bmatrix}, (j = 7 \sim 9) \tag{A5}$$

where $\left(x_{P,Wi\ or\ j}, y_{P,Wi\ or\ j}, z_{P,Wi\ or\ j}\right)$ and $\left(x_{Wi\ or\ j}, y_{Wi\ or\ j}, z_{Wi\ or\ j}\right)$ are the coordinates of the *i or j*− th hinged point in the body-fixed coordinate systems of the platform and the *i or j*− th WEC, respectively.

The PTO damping matrix $\boldsymbol{C_{PTO}}$ can be expressed as:

$$\boldsymbol{C_{PTO}} = \begin{bmatrix} \boldsymbol{C_{pto4}} & -\boldsymbol{C_{pto2}} & -\boldsymbol{C_{pto2}} & -\boldsymbol{C_{pto2}} & -\boldsymbol{C_{pto3}} & -\boldsymbol{C_{pto3}} & -\boldsymbol{C_{pto3}} & -\boldsymbol{C_{pto1}} & -\boldsymbol{C_{pto1}} & -\boldsymbol{C_{pto1}} \\ -\boldsymbol{C_{pto2}} & \boldsymbol{C_{pto2}} & \boldsymbol{0} & \boldsymbol{0} & \boldsymbol{0} & \boldsymbol{0} & \boldsymbol{0} & \boldsymbol{0} & \boldsymbol{0} & \boldsymbol{0} \\ -\boldsymbol{C_{pto2}} & \boldsymbol{0} & \boldsymbol{C_{pto2}} & \boldsymbol{0} & \boldsymbol{0} & \boldsymbol{0} & \boldsymbol{0} & \boldsymbol{0} & \boldsymbol{0} & \boldsymbol{0} \\ -\boldsymbol{C_{pto2}} & \boldsymbol{0} & \boldsymbol{0} & \boldsymbol{C_{pto2}} & \boldsymbol{0} & \boldsymbol{0} & \boldsymbol{0} & \boldsymbol{0} & \boldsymbol{0} & \boldsymbol{0} \\ -\boldsymbol{C_{pto3}} & \boldsymbol{0} & \boldsymbol{0} & \boldsymbol{0} & \boldsymbol{C_{pto3}} & \boldsymbol{0} & \boldsymbol{0} & \boldsymbol{0} & \boldsymbol{0} & \boldsymbol{0} \\ -\boldsymbol{C_{pto3}} & \boldsymbol{0} & \boldsymbol{0} & \boldsymbol{0} & \boldsymbol{0} & \boldsymbol{C_{pto3}} & \boldsymbol{0} & \boldsymbol{0} & \boldsymbol{0} & \boldsymbol{0} \\ -\boldsymbol{C_{pto3}} & \boldsymbol{0} & \boldsymbol{0} & \boldsymbol{0} & \boldsymbol{0} & \boldsymbol{0} & \boldsymbol{C_{pto3}} & \boldsymbol{0} & \boldsymbol{0} & \boldsymbol{0} \\ -\boldsymbol{C_{pto1}} & \boldsymbol{0} & \boldsymbol{0} & \boldsymbol{0} & \boldsymbol{0} & \boldsymbol{0} & \boldsymbol{0} & \boldsymbol{C_{pto1}} & \boldsymbol{0} & \boldsymbol{0} \\ -\boldsymbol{C_{pto1}} & \boldsymbol{0} & \boldsymbol{0} & \boldsymbol{0} & \boldsymbol{0} & \boldsymbol{0} & \boldsymbol{0} & \boldsymbol{0} & \boldsymbol{C_{pto1}} & \boldsymbol{0} \\ -\boldsymbol{C_{pto1}} & \boldsymbol{0} & \boldsymbol{0} & \boldsymbol{0} & \boldsymbol{0} & \boldsymbol{0} & \boldsymbol{0} & \boldsymbol{0} & \boldsymbol{0} & \boldsymbol{C_{pto1}} \end{bmatrix}_{(10\times6)\times(10\times6)} \tag{A6}$$

where,

$$\boldsymbol{C_{pto1}} = \begin{bmatrix} 0 & 0 & 0 & 0 & 0 & 0 \\ 0 & 0 & 0 & 0 & 0 & 0 \\ 0 & 0 & 0 & 0 & 0 & 0 \\ 0 & 0 & 0 & 0 & 0 & 0 \\ 0 & 0 & 0 & 0 & c_{p2} & 0 \\ 0 & 0 & 0 & 0 & 0 & 0 \end{bmatrix} \tag{A7}$$

$$\boldsymbol{C_{pto2}} = \begin{bmatrix} 0 & 0 & 0 & 0 & 0 & 0 \\ 0 & 0 & 0 & 0 & 0 & 0 \\ 0 & 0 & 0 & 0 & 0 & 0 \\ 0 & 0 & 0 & \frac{3}{4}c_{p1} & \frac{\sqrt{3}}{4}c_{p1} & 0 \\ 0 & 0 & 0 & \frac{\sqrt{3}}{4}c_{p1} & \frac{1}{4}c_{p1} & 0 \\ 0 & 0 & 0 & 0 & 0 & 0 \end{bmatrix} \tag{A8}$$

$$\boldsymbol{C_{pto3}} = \begin{bmatrix} 0 & 0 & 0 & 0 & 0 & 0 \\ 0 & 0 & 0 & 0 & 0 & 0 \\ 0 & 0 & 0 & 0 & 0 & 0 \\ 0 & 0 & 0 & \frac{3}{4}c_{p1} & -\frac{\sqrt{3}}{4}c_{p1} & 0 \\ 0 & 0 & 0 & -\frac{\sqrt{3}}{4}c_{p1}0 & \frac{1}{4}c_{p1} & 0 \\ 0 & 0 & 0 & 0 & 0 & 0 \end{bmatrix} \tag{A9}$$

$$\boldsymbol{C_{pto4}} = 3\left(\boldsymbol{C_{pto1}} + \boldsymbol{C_{pto2}} + \boldsymbol{C_{pto3}}\right) = \begin{bmatrix} 0 & 0 & 0 & 0 & 0 & 0 \\ 0 & 0 & 0 & 0 & 0 & 0 \\ 0 & 0 & 0 & 0 & 0 & 0 \\ 0 & 0 & 0 & c_{p-1} & 0 & 0 \\ 0 & 0 & 0 & 0 & c_{p-2} & 0 \\ 0 & 0 & 0 & 0 & 0 & 0 \end{bmatrix}, \textit{where } c_{p-1} = \frac{9}{2}c_{p1}, \textit{and } c_{p-2} = \frac{3}{2}c_{p1} + 3c_{p2} \tag{A10}$$

where c_{p1} is the PTO damping coefficient of the individual WEC among Rows1&2, and c_{p2} is the PTO damping coefficient of the individual WEC among Row 3.

In fact, C_{pto2} and C_{pto3} can be derived based on Eqs. (A11)-(A12),

$$\boldsymbol{T}_1^{'}\begin{bmatrix}\boldsymbol{C} & -\boldsymbol{C}\\ -\boldsymbol{C} & \boldsymbol{C}\end{bmatrix}\boldsymbol{T}_1=\begin{bmatrix}\boldsymbol{C}_{pto2} & -\boldsymbol{C}_{pto2}\\ -\boldsymbol{C}_{pto2} & \boldsymbol{C}_{pto2}\end{bmatrix} \tag{A11}$$

$$\boldsymbol{T}_2^{'}\begin{bmatrix}\boldsymbol{C} & -\boldsymbol{C}\\ -\boldsymbol{C} & \boldsymbol{C}\end{bmatrix}\boldsymbol{T}_2=\begin{bmatrix}\boldsymbol{C}_{pto3} & -\boldsymbol{C}_{pto3}\\ -\boldsymbol{C}_{pto3} & \boldsymbol{C}_{pto3}\end{bmatrix} \tag{A12}$$

where,

$$\boldsymbol{C}=\begin{bmatrix}0&0&0&0&0&0\\0&0&0&0&0&0\\0&0&0&0&0&0\\0&0&0&0&0&0\\0&0&0&0&c_{p1}&0\\0&0&0&0&0&0\end{bmatrix} \tag{A13}$$

$$\boldsymbol{T}_1=\begin{bmatrix}\lambda_1&&&\\&\lambda_1&&\\&&\lambda_1&\\&&&\lambda_1\end{bmatrix} \tag{A14}$$

$$\boldsymbol{T}_2=\begin{bmatrix}\lambda_2&&&\\&\lambda_2&&\\&&\lambda_2&\\&&&\lambda_2\end{bmatrix} \tag{A15}$$

Notably, λ is the direction cosine matrix of the local coordinate system that corresponding to the global coordinate system. Wherein, λ_1 and λ_2 are for the individual WECs among Row1 and Row2, respectively. Therefore,

$$\lambda_1=\begin{bmatrix}cos\,60^\circ & cos\,150^\circ & cos\,90^\circ\\ cos\,30^\circ & cos\,60^\circ & cos\,90^\circ\\ cos\,90^\circ & cos\,90^\circ & cos\,0^\circ\end{bmatrix} \tag{A16}$$

$$\lambda_2=\begin{bmatrix}cos\,60^\circ & cos\,30^\circ & cos\,90^\circ\\ cos\,150^\circ & cos\,60^\circ & cos\,90^\circ\\ cos\,90^\circ & cos\,90^\circ & cos\,0^\circ\end{bmatrix} \tag{A17}$$

As for the mean captured power of the WECs among different rows, the calculation formula can be derived based on Section 2.4:

First, for the individual WEC among Row1,

$$P_M^{'}=\frac{1}{T}\int_t^{t+T}\left[\left|\tau_{P,Wi}^r\left(\dot{\theta}_P^r-\dot{\theta}_{Wi}^r\right)\right|+\left|\tau_{P,Wi}^p\left(\dot{\theta}_P^p-\dot{\theta}_{Wi}^p\right)\right|\right]dt,\ (i=1\sim 3) \tag{A18}$$

$$\tau_{P,Wi}^r=\frac{3}{4}c_{p1}\left(\dot{\theta}_P^r-\dot{\theta}_{Wi}^r\right)+\frac{\sqrt{3}}{4}c_{p1}\left(\dot{\theta}_P^p-\dot{\theta}_{Wi}^p\right) \tag{A19}$$

$$\tau_{P,Wi}^p=\frac{\sqrt{3}}{4}c_{p1}\left(\dot{\theta}_P^r-\dot{\theta}_{Wi}^r\right)+\frac{1}{4}c_{p1}\left(\dot{\theta}_P^p-\dot{\theta}_{Wi}^p\right) \tag{A20}$$

where $\tau_{P,Wi}^r$ and $\tau_{P,Wi}^r$ are the roll and pitch torques of the PTO system, respectively, which act on the platform and the $i-$ th WEC; $\dot{\theta}_P^r$ and $\dot{\theta}_{Wi}^r$ are the roll angular velocity of the platform and the $i-$ th WEC, respectively; $\dot{\theta}_P^p$ and $\dot{\theta}_{Wi}^p$ are the pitch angular velocity of the platform and the $i-$ th WEC, respectively.

Then, for the individual WEC among Row2,

$$P_M^{'}=\frac{1}{T}\int_t^{t+T}\left[\left|\tau_{P,Wj}^r\left(\dot{\theta}_P^r-\dot{\theta}_{Wj}^r\right)\right|+\left|\tau_{P,Wj}^p\left(\dot{\theta}_P^p-\dot{\theta}_{Wj}^p\right)\right|\right]dt,\ (j=4\sim 6) \tag{A21}$$

$$\tau_{P,Wj}^r=\frac{3}{4}c_{p1}\left(\dot{\theta}_P^r-\dot{\theta}_{Wj}^r\right)-\frac{\sqrt{3}}{4}c_{p1}\left(\dot{\theta}_P^p-\dot{\theta}_{Wj}^p\right) \tag{A22}$$

$$\tau_{P,Wj}^{p} = -\frac{\sqrt{3}}{4}c_{p1}\left(\dot{\theta}_{P}^{r} - \dot{\theta}_{Wj}^{r}\right) + \frac{1}{4}c_{p1}\left(\dot{\theta}_{P}^{p} - \dot{\theta}_{Wj}^{p}\right) \tag{A23}$$

Lastly, for the individual WEC among Row3,

$$P_{M}^{'} = \frac{1}{T}\int_{t}^{t+T}\left|\tau_{P,Wk}^{p}\left(\dot{\theta}_{P}^{p} - \dot{\theta}_{Wk}^{p}\right)\right|dt, (k = 7 \sim 9) \tag{A24}$$

$$\tau_{P,Wk}^{p} = c_{p2}\left(\dot{\theta}_{P}^{p} - \dot{\theta}_{Wk}^{p}\right) \tag{A25}$$

References

Barltrop, N.D.P., 1998. Floating Structures: a Guide for Design and Analysis, vol. 1. CMPT and OPL.

Cao, Q., Xiao, L., Cheng, Z., Liu, M., 2021. Dynamic responses of a 10 MW semi-submersible wind turbine at an intermediate water depth: a comprehensive numerical and experimental comparison. Ocean. Eng. 232, 109138.

Cao, Q., Xiao, L., Cheng, Z., Liu, M., Chen, Y., Zhang, K., 2023. Research on the conceptual design and performance analysis of a 10 MW SPIC concept floating wind turbine foundation in intermediate water depth. J. Renew. Sustain. Energy 15, 063303.

Chandrasekaran, S., Sricharan, V.V.S., 2021. Numerical study of bean-float wave energy converter with float number parametrization using WEC-Sim in regular waves with the Levelized Cost of Electricity assessment for Indian sea states. Ocean. Eng. 237, 109591.

Choupin, Q., Del Río-Gamero, B., Schallenberg-Rodríguez, J., Yanez-Rosales, P., 2022. Integration of assessment-methods for wave renewable energy: resource and installation feasibility. Renew. Energy 185, 455–482.

Deng, S., Xu, Y., Ren, H., Fu, S., Li, S., Moan, T., Gao, Z., 2022. Numerical simulation of wave-induced hydroelastic response and flow-induced vibration of a twin-tube submerged floating tunnel. Mar. Struct. 82, 103124.

Faltinsen, O.M., 1993. Sea Loads on Ships and Offshore Structures, vol. 1. Cambridge University Press.

Ghafari, H.R., Ghassemi, H., Abbasi, A., Vakilabadi, K.A., Yazdi, H., He, G., 2022. Novel concept of hybrid wavestar- floating offshore wind turbine system with rectilinear arrays of WECs. Ocean. Eng. 262, 112253.

Ghafari, H.R., Ghassemi, H., He, G., 2021. Numerical study of the Wavestar wave energy converter with multi-point-absorber around DeepCwind semisubmersible floating platform. Ocean. Eng. 232, 109177.

Göteman, M., McNatt, C., Giassi, M., Engström, J., Isberg, J., 2018. Arrays of point-absorbing wave energy converters in short-crested irregular waves. Energies 11, 964.

Hall, M., Goupee, A., 2015. Validation of a lumped-mass mooring line model with DeepCwind semisubmersible model test data. Ocean. Eng. 104, 590–603.

He, G., Liu, C., Zhang, W., Luan, Z., Zhang, Z., 2023. Numerical study of the effect of central platform motion on the wave energy converter array. Ocean. Eng. 286, 115483.

Ji, X., Liu, S., Bingham, H.B., Li, J., 2015. Multi-directional random wave interaction with an array of cylinders. Ocean. Eng. 110, 62–77.

Jiao, J., Chen, C., Ren, H., 2019. A comprehensive study on ship motion and load responses in short-crested irregular waves. Int. Nav. Arch. Ocean 11, 364–379.

Jin, P., Zheng, Z., Zhou, Z., Zhou, B., Wang, L., Yang, Y., Liu, Y., 2023. Optimization and evaluation of a semi-submersible wind turbine and oscillating body wave energy converters hybrid system. Energy 282, 128889.

Lee, S., Kim, C., Paik, K., Kim, H., Chun, J., 2024. A numerical study of added resistance performance and hydrodynamics of KCS hull in oblique regular waves and estimation of resistance in short-crested irregular waves through spectral method. Int. Nav. Arch. Ocean 16, 100563.

Li, L., Liu, Y., 2022. Short-crestedness effect on the dynamic response of offshore floating wind turbines. Ships offshore struc 17 (10), 2272–2281.

Li, S., Moan, T., Fu, S., Zhang, S., Xu, Y., 2023. Hydroelastic analysis of a floating bridge under spatially inhomogeneous waves, with emphasis on the effect of drift force modeling. Appl. Ocean Res. 139, 103666.

Li, Y., Yu, Y., 2012. A synthesis of numerical methods for modeling wave energy converter-point absorbers. Renew. Sustain. Energy Rev. 16 (6), 4352–4364.

Molin, B., 2022. Offshore Structure Hydrodynamics. Cambridge University Press.

Newman, J.N., 1974. Second order slowly varying forces on vessels in irregular waves. In: Symposium on Dynamics of Marine Vehicles and Structures in Waves, pp. 182–186.

Nguyen, H.P., Wang, C.M., Tay, Z.Y., Luong, V.H., 2020. Wave energy converter and large floating platform integration: a review. Ocean. Eng. 213, 107768.

Ning, D., Deng, S., Liu, Y., Zhou, Y., Chen, L., 2024. Floating wind turbine response in uni- and multi-directional nonlinear waves by numerical and experimental investigations. Phys. Fluids 36, 067136.

Rony, J.S., Karmakar, D., 2024. Hydrodynamic response analysis of a hybrid TLP and heaving-buoy wave energy converter with PTO damping. Renew. Energy 226, 120380.

Sørum, S.H., Krokstad, J.R., Amdahl, J., 2019. Wind-wave directional effectson fatigue of bottom-fixed offshore wind turbine. J. Phys. Conf. Ser. 1356, 012011.

Viuff, T., Leira, B.J., Xiang, X., Øiseth, O., 2019. Effects of wave directionality onextreme response for a long end-anchored floating bridge. Appl. Ocean Res. 90, 101843.

Wei, Z., Shi, H., Cao, F., Yu, M., Li, M., Chen, Z., Liu, P., 2024. Study on the power performance of wave energy converters mounted around an offshore wind turbine jacket platform. Renew. Energy 221, 119786.

Wu, H., Zhu, F., Yuan, Z., 2024. Effects of the WEC shape on the performance of a novel hybrid WEC-FOWT system. Energy 288, 129907.

Yue, M., Liu, Q., Ding, Q., Cheng, S., Zhu, H., 2020. Effects of heave plate on dynamic response of floating wind turbine Spar platform under the coupling effect of wind and wave. Ocean. Eng. 201, 107103.

Zhang, H., Xu, D., Liu, C., Wu, Y., 2016. Wave energy absorption of a wave farm with an array of buoys and flexible runway. Energy 109, 211–223.

Zhang, H., Xu, D., Zhao, H., Xia, S., Wu, Y., 2018. Energy extraction of wave energy converters embedded in a very large modularized floating platform. Energy 158, 317–329.

Zhang, L., Zhang, J., Shang, Y., 2021. A practical direct URANS CFD approach for the speed loss and propulsion performance evaluation in short-crested irregular head waves. Ocean. Eng. 219, 108287.

Zhang, X., Tian, X., Xiao, L., Li, X., Lu, W., 2019. Mechanism and sensitivity for broadband energy harvesting of an adaptive bistable point absorber wave energy converter. Energy 188, 115984.

Zhang, Z., Chen, X., Wu, H., Liu, W., Cui, L., 2023. Numerical study of a novel hybrid system with the Wavestar wave energy converter array and a SPIC semi-submersible floating platform. J. Clean. Prod. 407, 137178.

Zhao, X., Xue, F., Chen, L., Göteman, M., Han, D., Geng, J., Sun, S., 2023. Hydrodynamic analysis of a floating platform coupled with an array of oscillating bodies. Ocean. Eng. 287, 115439.

Zhou, B., Hu, J., Sun, K., Liu, Y., Collu, M., 2020. Motion response and energy conversion performance of a heaving point absorber wave energy converter. Front. Energy Res. 8, 553295.

Zhou, B., Zheng, Z., Hong, M., Jin, P., Wang, L., Chen, F., 2023. Dynamic and power generation features of A Wind−Wave hybrid system consisting of A spar-type wind turbine and an annular wave energy converter in irregular waves. China Ocean Eng. 37 (6), 923–933.

Zhu, K., Shi, H., Zheng, S., Michele, S., Cao, F., 2023. Hydrodynamic analysis of hybrid system with wind turbine and wave energy converter. Appl. Energy 350, 121745.